Remote Sensing of Environment 295 (2023) 113698

Contents lists available at ScienceDirect

Remote Sensing of Environment

journal homepage: www.elsevier.com/locate/rse

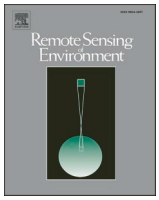

Detection of symptoms induced by vascular plant pathogens in tree crops using high-resolution satellite data: Modelling and assessment with airborne hyperspectral imagery

T. Poblete [a], J.A. Navas-Cortes [b], A. Hornero [b,a], C. Camino [c], R. Calderon [d], R. Hernandez-Clemente [e,f], B.B. Landa [b], P.J. Zarco-Tejada [a,b,*]

[a] School of Agriculture and Food (SAF-FVAS) and Faculty of Engineering and Information Technology (IE-FEIT), University of Melbourne, Melbourne, Victoria, Australia
[b] Instituto de Agricultura Sostenible (IAS), Consejo Superior de Investigaciones Científicas (CSIC), Avda. Menéndez Pidal s/n, 14004 Córdoba, Spain
[c] European Commission, Joint Research Centre (JRC), Ispra, Italy
[d] Plant Pathology and Plant-Microbe Biology Section, School of Integrative Plant Science, Cornell AgriTech, Cornell University, Geneva, NY, USA
[e] Department of Geography, Swansea University (SU), SA2 8PP Swansea, United Kingdom
[f] Department of Forestry Engineering, Universidad de Córdoba (UCO), N-IV, km 396, 14014 Córdoba, Spain

ARTICLE INFO

Edited by Jing M. Chen

Keywords:
Hyperspectral
Multispectral
Worldview-2 and -3
Plant traits
Operational plant disease detection
Verticillium dahliae
Xylella fastidiosa
Olive
Almond

ABSTRACT

Infection by the fungus *Verticillium dahliae* (*Vd*) and the bacterium *Xylella fastidiosa* (*Xf*) threatens the production of olives (*Olea europaea* L.) and almonds (*Prunus dulcis* Mill.) worldwide. Producing symptoms that resemble water stress or nutrient deficiency, infection by these vascular pathogens restricts water and nutrient flow through the xylem. Hyperspectral, narrow-band multispectral, and thermal imagery acquired at a high spatial resolution can detect disease symptoms, even before they are visible, potentially allowing growers to distinguish infected plants from those affected by confounding environmental stresses. Nevertheless, operational detection of vascular disease using high-resolution commercial satellite multispectral images remains to be evaluated. Here, we assessed the capacity of high-resolution Worldview-2 and -3 multispectral imagery to detect *Xf* and *Vd* infections in olive and almond orchards in Spain, Italy, and Australia between 2011 and 2021. We compared the accuracy of detecting both pathogens using the satellite imagery with results obtained using aerial high-resolution hyperspectral and thermal imaging, with model-inverted plant traits, solar-induced chlorophyll fluorescence (SIF), and thermal data as a reference. Our results using spectral plant traits to examine disease progression at all stages showed that traits and their importance varied as a function of disease severity. Worldview-2 and -3 detected the disease incidence with overall accuracies ranging from 0.63 to 0.83 and *kappa* coefficients (κ) ranging from 0.29 to 0.68. Nevertheless, detecting the early stages of disease with multispectral satellite data yielded poorer results, with κ values of 0.22–0.45, compared with κ values of 0.3–0.69 obtained from hyperspectral data. Typical multispectral bandsets available from satellite sensors cannot measure important plant traits such as the blue index NPQI, xanthophyll proxy PRI_n, SIF, and anthocyanin levels, thus explaining the poorer results obtained from multispectral satellite data for the early detection of vascular diseases. Adding a thermal-based crop water stress indicator to the satellite data improved the overall accuracies by 10–15% and increased κ by >0.2 units. This work shows that commercial multispectral high-spatial resolution imagery can be used to detect intermediate and advanced *Xf* and *Vd* infection, but that the early detection of disease symptoms requires hyperspectral and thermal data.

1. Introduction

Cultivation of olives (*Olea europaea* L.) and almonds (*Prunus dulcis* Mill.) has major socioeconomic importance worldwide (Özcan, 2022; Rallo et al., 2018). For example, in Spain, olives and almonds are first and second in acreage among crops (López-Moral et al., 2017). Almonds

* Corresponding author at: School of Agriculture and Food (SAF-FVAS) and Faculty of Engineering and Information Technology (IE-FEIT), University of Melbourne, Melbourne, Victoria, Australia.
E-mail address: pablo.zarco@unimelb.edu.au (P.J. Zarco-Tejada).

https://doi.org/10.1016/j.rse.2023.113698
Received 25 August 2022; Received in revised form 27 May 2023; Accepted 21 June 2023
Available online 27 June 2023

are cultivated in the USA, Australia, and Spain (Moral et al., 2019), and olives are grown in the Mediterranean region (Rallo et al., 2018), particularly Spain, Italy, and Greece, and in Argentina, where olive groves cover >110,000 ha (Torres et al., 2017). However, >100 pests and pathogens threaten almond and olive cultivation (Fernández-Escobar et al., 2013). One of the greatest threats worldwide is the gram-negative bacterium *Xylella fastidiosa* (*Xf*), which infects over 655 plant species (EFSA, 2022), including olive and almond. Another major threat is the soil-borne fungus *Verticillium dahliae* (*Vd*) Kleb, which threatens olive and almond production worldwide (Jimenez-Diaz et al., 2012; Luisi et al., 1993).

Early detection of infection allows growers to take measures against these devastating pathogens. However, traditional methods for detecting *Vd* and *Xf* infections involve in-situ observations followed by laboratory analysis that, despite being accurate, are time-consuming, labour-intensive, and expensive (Gramaje et al., 2013). Moreover, visible symptoms of vascular disease emerge well after the infection has been established and can be confused with symptoms of environmental stresses, such as water and nutrient deficiency.

Advanced imaging spectroscopy is crucial for the early detection of infections on a large scale, even before visible symptoms appear (Zarco-Tejada et al., 2018). Combining hyperspectral and thermal sensors on drones and piloted aircraft was an effective approach for detecting symptoms in *Vd*-infected olive trees at both the orchard- and large-scale levels (Calderón et al., 2013, 2015). These studies highlight the importance of temperature-based indicators such as air–canopy temperature difference (T_c—T_a) or crop water stress index (CWSI) (Idso et al., 1981) and solar-induced chlorophyll fluorescence (SIF) emission (Plascyk, 1975) for the early detection of biotic-induced symptoms. Additionally, data collected by narrow-band hyperspectral and thermal imaging sensors successfully could be combined to detect non-visual symptoms caused by *Xf* infection in olive trees (Zarco-Tejada et al., 2018). Using a machine learning approach that accounted for pigment, structural, fluorescence, and thermal-based plant traits (PSFTs), we could detect *Xf* infections with overall accuracy exceeding 80%. In this PSFT modelling scheme, the anthocyanins (Anth), SIF, normalized phaeophytinization index (NPQI) (Barnes et al., 1992; Peñuelas et al., 1995a, 1995b), and CWSI were the most critical spectral traits for detection of infected trees irrespective of infection severity. We then disentangled the symptoms triggered by *Xf* and *Vd* infections from the confounding responses induced by water stress (Zarco-Tejada et al., 2021); the accuracies, measured against qPCR analyses, exceeded 90% after the abiotic stress–induced responses were accounted for. A further refinement using a three-stage method was proposed to improve the detection and differentiation of symptoms caused by *Vd* and *Xf* infection, which can result in similar visual symptoms. This methodology enabled the detection and differentiation of *Vd* and *Xf* infections from a mixed (*Xf* + *Vd*) dataset with 98% and 92% accuracy, respectively (Poblete et al., 2021).

The performances of these models rely on high-spatial-resolution hyperspectral and thermal imagery to elucidate subjacent physiological changes affecting plant traits. Several studies have explored whether *Vd* and *Xf* infections could be detected at different scales and spatial resolutions (based on various technical and scientific innovations), which sets the stage for implementing these models on a global scale. Rey et al. (2019) demonstrated the effectiveness of a multi-sensor configuration system prototype that included an eight-band multispectral sensor, a low-cost hyperspectral spectrometer, a thermal camera, a LiDAR sensor, and two red-green-blue (RGB) cameras. The authors mounted this system onto an automated robot to monitor the various stages of disease progression in *Xf*-infected olive trees. Di Nisio et al. (2020) employed a five-band multispectral camera, an RGB camera, and thermal cameras mounted on an unmanned aerial vehicle (UAV) to detect *Xf*-induced symptoms in olive trees. These authors developed a segmentation algorithm coupled with linear discriminant analysis to differentiate between healthy and infected trees, reaching an accuracy of 93%. Castrignanò et al. (2021) used a four-band multispectral camera and a maximum likelihood classification algorithm to detect *Xf*-infected olive trees, showing an overall accuracy of 69% for all stages of the disease and 77% for the early stages.

The aforementioned studies utilized hyperspectral or narrow-band multispectral imagery captured by UAVs or piloted aircraft systems at a high spatial resolution. Upscaling these airborne-based models to satellite data resolution would allow global disease monitoring and forecasting. On that front, Hornero et al. (2020) proposed a hybrid 3D radiative transfer model for spatial and temporal analysis of *Xf* infections in olive orchards, assessing Sentinel-2 satellite images and using airborne hyperspectral images to validate >3000 olive trees affected by *Xf* in Puglia. Their findings demonstrated that the atmospherically resistant vegetation index (ARVI; Bannari et al., 1995) and the optimized soil-adjusted vegetation index (OSAVI; Rondeaux et al., 1996) could be used to track the temporal dynamics of both the incidence and severity of infection with accuracies of $R^2 = 0.71$ and 0.74. In that work, they tracked the understory reflectance time series recorded for all orchards monitored. Shortly after, Huang et al. (2021) employed MODIS NDVI data at a spatial resolution of 250 m to evaluate the spread of poplar looper (*Apocheima cinerarius*) on Euphrates or desert poplars (*Populus euphratica*) in China. By applying wavelet transformation and linear discriminant analysis techniques, the authors successfully identified pest infestations and forecasted their severity at over 36 sites monitored between 2009 and 2014. The severity prediction achieved an accuracy of 77.14% when tested on datasets not used for model training, while the detection of outbreak time achieved an accuracy of over 90%. Li et al. (2022) used simulations of an extended stochastic radiative transfer model on Sentinel-2 images to detect pine wilt disease (PWD) in pine forests with limited prior field data and multispectral and RGB imagery. The authors employed random forest (RF) algorithms to estimate infected areas on simulated data with an R^2 of 0.88. However, when applied to real data, the performance decreased to R^2 values ranging from 0.48 to 0.57.

Advances in plant disease detection using multispectral satellite imagery have been essential for developing large-scale operational models. However, it has been shown that the spectral Contribution of canopy components such as soil or scrub in medium-resolution pixels (10–60 m/px) constrains the quantification of plant traits necessary for early disease detection (Hornero et al., 2020). However, it is unclear whether satellite data with high spatial resolution could improve the detection of *Xf* and *Vd* infections in orchard trees. Furthermore, an assessment of the ability to track the subtle physiological changes triggered at the earliest stages of the disease progression comparing multispectral and hyperspectral-derived data has not been addressed yet. A pair of studies have made initial tests of the effects of the spectral reduction in the detection of *Xf* infections in olive trees (Poblete et al., 2020) and of trunk disease in grapevine (Bendel et al., 2020). Poblete et al. (2020) found that using the six most sensitive spectral bands coupled with CWSI resulted in a decrease in detection accuracy from 80% to 74% compared with the hyperspectral-derived data, showing that the addition of CWSI is critical for disease detection. However, it is important to note that this study only evaluated a theoretical reduction in spectral bands and did not investigate the use of actual satellite imagery. Later, Bendel et al. (2020) evaluated non-destructive sampling using ground-based hyperspectral and UAV multispectral images to detect the grapevine trunk disease Esca affecting vineyards. With ground-hyperspectral data, the detection of pre-symptomatic plants was possible, with accuracies ranging between 73 and 81% when using VNIR and between 79 and 91% when adding the SWIR spectral region. However, despite the accuracies obtained when using these ground measurements, the authors showed that when using multispectral images, the predictions were highly compromised, with accuracies only between 58% and 60% for detecting early infection symptoms. Mantas et al. (2022) proposed an RF algorithm to detect PWD-compatible decline in maritime pines using a combined dataset with Sentinel-2

and Worldview-3 images, reaching overall accuracies of 95%. However, this type of approach successfully applied for a PWD with a primary effect of discoloration and defoliation of tree crowns might be insufficient for *Xf* and *Vd* infections, which mainly affect the vegetation's functionality.

Here, we reasoned that higher spatial and spectral resolution satellite images might reduce the influence of the ground on spectral signatures and, as a result, improve the detection of vascular disease–induced stress compared to medium- and low-spatial-resolution images. The present study focuses on the effect of using high-resolution multispectral Worldview 2 and 3 satellite imagery, with high-resolution hyperspectral and thermal imagery as a benchmark. Furthermore, it progresses on understanding the underlying physiological changes reported by spectral analysis as a function of biotic stress, assessing the progression of the contributions of different plant traits retrieved by hyperspectral analysis to detect early, middle, and all levels of symptoms severity.

2. Materials and methods

2.1. Study sites

This study consisted of multi-date, −site, and -species monitoring comprising disease assessment data obtained from *Xf* outbreaks in Italy and Spain as well as *Vd* outbreaks in Spain and Australia.

The study sites to assess *Xf* infections affecting olive trees were located in Puglia, Italy and were monitored during 2016 and 2017, while the study sites to monitor the disease progress affecting almond trees were located in Majorca (Balearic islands), Spain in 2019 and 2021. The study sites to study *Vd* infections were located in Castro, Spain and in Australia which were monitored in 2011 and 2020–2021, respectively. Visual assessments of the disease severity (SEV) were performed using a scale of 0–4 based on the percentage of the tree canopy showing disease symptoms between 2011 and 2022 in olive and almond orchards affected by *Xf* and *Vd* pathogens (Table 1).

2.1.1. Study sites with Vd infections in olive trees

Visual assessments of *Vd* infections were conducted in olive orchards located in Spain and Australia during 2011–2013 and 2020–2022, respectively (detailed field data used in this study regarding *Vd* outbreaks in Spain were reported by Calderón et al., 2013, 2015). The site monitored in 2011 was in Castro del Rio (Córdoba, Spain) and comprised olive trees of cv. Picual (Calderón et al., 2013), while in 2013 the study site was located in Ecija (Seville, Spain) and comprised olive trees of cvs. Picual and Hojiblanca (Calderón et al., 2015). The area of the olive orchards assessed during these campaigns ranged between 1.69 and 7.28 ha. In the Castro study site, 1878 olive trees were assessed, among which 1569 were asymptomatic (SEV = 0) and 283 were symptomatic (77%, SEV = 1; 16%, SEV = 2; 4%, SEV = 3 and 3%, SEV = 4; Fig. 1A). In the Ecija study site, visual assessments of SEV was performed for 5223 olive trees; 5040 trees were asymptomatic and 183 were symptomatic (61%, SEV = 1; 22%, SEV = 2; 12%, SEV = 3; and 5%, SEV = 4).

The study site monitored during 2020–2022 in Australia comprised olive trees of cvs. Koroneiki, Manzanillo, Picholine, Arbosana, Arbequina, Hojiblanca, Coratina, and Picual. The area covered by the orchards ranged between 44.9 and 456 ha. During the 2020–2021 growing season, 1036 olive trees were assessed, with 355 reported as asymptomatic and 681 as symptomatic (42%, SEV = 1; 18%, SEV = 2; 23%, SEV = 3 and 17%, SEV = 4). In addition, during the 2021–2022 growing season, 1296 olive trees were assessed, with 258 were reported as asymptomatic and 1038 as symptomatic (23%, SEV = 1; 27%, SEV = 2; 27%, SEV = 3; and 23%, SEV = 4; Fig. 1B).

2.1.2. Study sites with Xf infection in olive and almond trees

Visual inspection of *Xf* symptoms was conducted in olive and almond orchards located in Italy and Spain during 2016–2017, and 2019 and 2021, respectively (detailed field data used in this study regarding *Xf* outbreaks in Italy and Spain were reported by Zarco-Tejada et al., 2018 and 2021, and Poblete et al., 2020 and 2021). The study sites monitored in 2016 and 2017 were in Apulia (southern Italy) comprising olive trees of cv. Cellina di Nardò and cv. Ogliarola Salentina. For the field measurements, the area of the olive orchards ranged between 0.44 and 6.02 ha. The visual assessments were performed on 7296 olive trees. From this field campaign, 4045 trees were reported as asymptomatic and 3251 as symptomatic (45%, SEV = 1; 41%, SEV = 2; 11%, SEV = 3; and 3%, SEV = 4; Fig. 1C).

The study sites monitored in 2019 and 2021 were located in Majorca (Spain), comprising almond trees of cvs. Marinada, Soleta, Vairo, Ferragnes, and Marta. The areas of the orchards monitored were between 173 and 990 ha. The visual assessments carried out during 2019 showed that of 4048 almond trees assessed, 2661 were asymptomatic and 1387 were symptomatic (39%, SEV = 1; 32%, SEV = 2; 26%, SEV = 3; and 3%, SEV = 4; Fig. 1D). The visual assessments carried out on 2021 showed that from 2001 almond trees assessed, 1018 were asymptomatic while 983 where symptomatic (11%, SEV = 1; 16%, SEV = 2; 62%, SEV = 3; and 11%, SEV = 4).

Table 1
Description of the study sites, disease, affected species and number of trees included in this study.

Study site	Pathogen	Affected species	Year of data collection	Trees assessed
Puglia, Italy	*Xylella fastidiosa*	Olive trees	2016 and 2017	**7296:** - Asymptomatic (n = 4045) - Symptomatic (n = 3251)
Majorca, Spain	*Xylella fastidiosa*	Almond trees	2019 and 2021	**6049**: - Asymptomatic (n = 3679) - Symptomatic (n = 2370)
Castro, Spain	*Verticillium dahliae*	Olive trees	2011	**1878**: - Asymptomatic (n = 1569) - Symptomatic (n = 283)
Ecija, Spain	*Verticillium dahliae*	Olive trees	2013	**5223**: - Asymptomatic (n = 5040) - Symptomatic (n = 183)
Australia	*Verticillium dahliae*	Olive trees	2020 and 2021	**2332**: - Asymptomatic (n = 613) - Symptomatic (n = 1719)

2.2. Airborne hyperspectral and thermal imagery

Narrow-band hyperspectral and thermal imagery data were collected over all study sites concurrently with the field assessments. Details of the airborne campaigns were reported by Calderón et al. (2013 and 2015), Zarco-Tejada et al. (2018 and 2021), Hornero et al. (2020), and Poblete et al. (2020 and 2021). For the flight campaigns carried out in Italy and Spain, the narrow-band hyperspectral images consisted of 260 bands in the 400–885 nm spectral range collected with 6.4-nm of full-width at half maximum (FWHM) using a headwall Photonics (Fitchburg, MA, USA) VNIR linear hyperspectral sensor. This sensor has an 8-mm focal length that allows an angular field of view (FOV) of 50°. For the flight campaigns carried out during 2020–2022, narrow-band hyperspectral images comprising 371 bands in the 400–1000 spectral range were collected with 5.8-nm of FWHM using a hyperspectral imager (Hyperspec VNIR *E*-Series model, Headwall Photonics, Fitchburg, MA, USA).

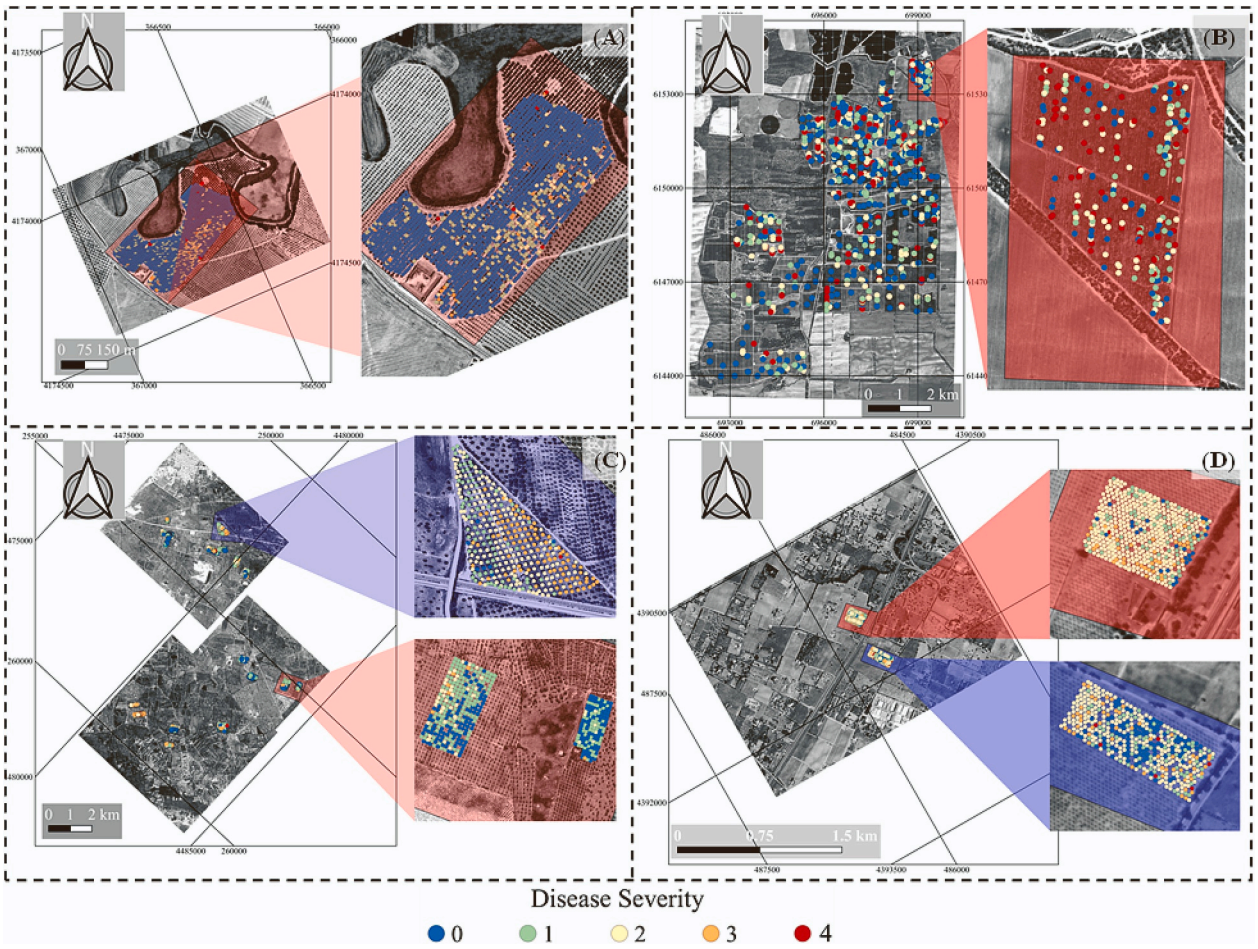

Fig. 1. Spatial distribution of visual assessments for *Xylella fastidiosa* (*Xf*) and *Verticillium dahliae* (*Vd*) infection performed between 2011 and 2022. (A) Castro, Spain site monitored in 2011 for *Vd* infections in olive trees. (B) Australia site monitored in 2020–2022 for *Vd* infections in olive trees. (C) Puglia, Italy site monitored in 2016–2017 for *Xf* infections in olive trees. (D) Majorca, Spain site monitored in 2019 and 2021 for *Xf* infections in almond trees.

This sensor has an 8-mm focal length that allows a FOV of 66°.

Radiometric calibration was performed on the hyperspectral imagery collected by both sensors, applying to each image the coefficients obtained from different illumination levels with a constant light source using a CSTM-USS-2000C and a SPARC-A060L integrating sphere (LabSphere, North Sutton, NH, USA) for the 6.4-nm and the 5.8-nm FWHM sensors, respectively. The atmospheric correction and irradiance calculation to convert radiance values to reflectance was conducted with the SMARTS model (Gueymard, 2001) using aerosol optical properties and meteorological parameters measured at the time of the image acquisition. The aerosol optical depth at 550 nm was derived using readings with a Microtops II sun photometer (Solar LIGHT Co., Philadelphia, PA, USA) at wavelengths 440, 500, 675, 870, and 936 nm, and the meteorological parameters were obtained using a portable weather station (Transmitter PTU30, Vaisala, Helsinki, Finland, for the data obtained in Spain and Italy; and WXT510, Vaisala, Helsinki, Finland, for the data obtained in Australia). The calibrated and atmospherically corrected hyperspectral images were ortho-rectified using the Parametric Geocoding & Ortho-rectification for Airborne Optical Scanner Data software (PARGE, ReSe Applications Schläpfer, Wil, Switzerland). This method uses as inputs the IMU and GPS information obtained from the solidly installed and synchronized inertial measurement units (IG500 model; SBG Systems, Carrières-sur-Seine, France, for the images collected in Italy and Spain; VN-300-VectorNav Technologies LLC, Dallas, TX, USA for the images collected in Australia).

High-resolution thermal imagery was collected using a thermal camera flown in tandem with the hyperspectral imager. A FLIR SC655c (FLIR Systems, USA) uncooled microbolometer covering the 7.5–14-μm spectral range with a spatial resolution of 640 × 480 pixels was used for all study sites. This sensor has a focal length of 24.6 mm f/1.0 allowing a FOV of 45°. Vicarious thermal calibration was performed using soil temperature measured for each flight as described by Calderón et al. (2013). To isolate individual tree crowns and obtain radiance, reflectance, and temperature from unmixed vegetation pixels, both Niblack's thresholding (Niblack, 1986) and Sauvola's binarization (Sauvola and Pietikäinen, 2000) methods were implemented to remove background, soil, and within-crown shadow pixels. Pure tree–crown thermal data were used for the calculation of CWSI (Idso et al., 1981), which is one of the most sensitive reported indicators of early symptoms for both *Xf* and *Vd* infection (Calderón et al., 2013 and 2015; Zarco-Tejada et al., 2018 and 2021; Poblete et al., 2021) due to its link with the reduction of transpiration rates.

The pure tree–crown radiance spectra were then used for quantification of sun-induced chlorophyll fluorescence at 760 nm ($SIF_{@760}$) using the O_2-A *in-filling* Fraunhofer Line Depth (FLD) method (Plascyk, 1975), which is also an indicator of *Xf*- and *Vd*-induced stress in both olives and almonds due to the reduction in photosynthesis experienced by the infected plants (Zarco-Tejada et al., 2018 and 2021).

The pure tree–crown reflectance spectra extracted from the images were used to calculate the set of narrow-band hyperspectral indices (NBHIs) for each tree identified in the images that corresponded with a tree evaluated in the field. The set of NBHIs selected (see full details of the hyperspectral indices in Zarco-Tejada et al., 2018 and 2021) required spectral bands in the VNIR spectral region and are related to

structural traits and concentration of plant pigments such as chlorophyll $a + b$, carotenoids, anthocyanins, and xanthophylls. In addition to the NBHI calculation, the leaf biochemical and canopy structural parameters were determined using the inversion of radiative transfer models described in Section 2.4.

2.3. Worldview-2 and -3 satellite imagery

High-spatial-resolution Worldview-2 (WV-2) and Worldview-3 (WV-3) images captured close to the dates of the hyperspectral and thermal airborne campaigns were acquired for all study sites (Table 2). Both platforms were launched by DigitalGlobe in October 2009 and August 2014 and operate in a sun-synchronous orbit. While both sensors capture spectral information in the VNIR collecting eight multispectral bands in the 400–1040-nm spectral range, WV-3 also captures eight SWIR bands in the 1195–2365-nm spectral range at a lower resolution. For this study, only the VNIR bands were used due to the low spatial resolution of the SWIR bands (3.7 m), which prevented the identification of pure tree crowns. WV-2 and WV-3 obtain panchromatic data at a ground sample distance of 0.46 and 0.31 m, respectively, and multispectral data in the VNIR region at 1.84 and 1.24 m, respectively. Despite the spatial resolution differences, the configuration of the spectral band centers of both sensors is similar, with eight multispectral bands in the visible region, including 400–450 nm (center wavelength, CWL = 427.3 nm), 450–510 nm (CWL = 477.9 nm), 510–580 nm (CWL = 546.2 nm), 585–625 nm (CWL = 607.8 nm), and 630–690 nm (CWL = 658.8 nm), along with one band in the red-edge at 705–745 nm (CWL = 723.7 nm) and two bands in the near-infrared at 770–895 nm (CWL = 832.5 nm) and 860–1040 nm (CWL = 908 nm). A comparison of the spatial resolution acquired by the satellite multispectral imagery and the airborne hyperspectral imagery used in this study can be found in Fig. 2.

2.3.1. Radiometric calibration and atmospheric correction of Worldview imagery

WV-2 and WV-3 products were provided by the vendor as radiometrically calibrated and atmospherically corrected image pixels with top-of-atmosphere (TOA) reflectance. However, that processing level does not consider topographic, atmospheric, or BRDF differences (Richards, 1999). Therefore, to allow a quantitative analysis comparable with that from surface measurements, all images provided from WV-2 and WV-3 satellites were atmospherically corrected (bottom of atmosphere [BOA]) using the empirical line method prior to data extraction for subsequent analyses. This technique has been successfully applied to both aerial data and coarser spatial resolution satellite sensor data (Karpouzli and Malthus, 2003). Here, we performed this cross-calibration with Sentinel-2 imagery using homogeneous and time-invariant calibration zones.

The high spatial resolution of Worldview and Sentinel-2 images allowed us to identify areas of bare soil to be used as homogeneous calibration objects. Sentinel-2 imagery was selected by searching for the closest cloud-free date within the location of each study area. Once the area was established, the images were downloaded at the L1C processing level to be processed to Surface Reflectance (L2A) using Sen2Cor (Main-Knorn et al., 2017). To obtain the synthetic-target bare soil for the Worldview spectral bands, a third-degree polynomial interpolation was performed for each study area and collection date. The coefficients of determination of the observed prediction equations for each zone were reasonably high ($R^2 > 0.95$). Finally, to compute the empirical line factors, the source spectral data (TOA) were forced to match the target spectral data (synthetic values extracted from the previous step, BOA) using linear regression to match each band to the target reflectance (Fig. 3).

In addition to the NBHI calculated from the narrow-band hyperspectral images, multispectral indices (Sagan et al., 2021) were calculated from the Worldview satellite imagery (Table 3) to compare the differences between asymptomatic trees (SEV = 0) and the different disease severity levels (SEV = 1, SEV = 2, SEV = 3, and SEV = 4); an analysis of variance (ANOVA), followed by a Dunnett's test was performed at $\alpha < 0.05$.

Table 2
Description of the satellite and airborne imagery collected in this study.

Study site	Outbreak assessed	Imagery collected	Date of collection
Xylella fastidiosa datasets			
Apulia, Italy	*Xylella fastidiosa*	Narrow-band hyperspectral and thermal	June 2016–July 2017
		Worldview-2	August 2017
Majorca, Spain	*Xylella fastidiosa*	Narrow-band hyperspectral and thermal	July 2019
		Worldview-2	May-Sept 2019
		Worldview-3	July-Sept 2019
Majorca, Spain	*Xylella fastidiosa*	Narrow-band hyperspectral and thermal	July 2021
		Worldview-2	July–August 2021
		Worldview-3	July 2021
Verticillium dahliae datasets			
Castro, Spain	*Verticillium dahliae*	Narrow-band hyperspectral and thermal	June 2011
		Worldview-2	June 2011
Australia	*Verticillium dahliae*	Narrow-band hyperspectral and thermal	November 2020
		Worldview-3	November 2020
		Narrow-band hyperspectral and thermal	December 2021
		Worldview-3	December 2021

2.4. Modelling methods

Leaf biochemical constituents and canopy structural properties were retrieved using an inversion approach based on the PRO4SAIL radiative transfer model (as in Zarco-Tejada et al., 2018 and Zarco-Tejada et al., 2021, Poblete et al., 2021). PRO4SAIL couples the PROSPECT-D (Féret et al., 2017) leaf radiative transfer model and the 4SAIL (Verhoef et al., 2007) canopy radiative transfer model. Leaf pigments such as chlorophyll $a + b$ (C_{a+b}), anthocyanins (Anth.), and carotenoids (C_{x+c}) were quantified using the modelling approach since they are important for predicting symptoms caused by infection by *Xf* and *Vd* in almond and olive species (Zarco-Tejada et al., 2018, 2021). Structural traits including the leaf inclination distribution function (LIDF) and the leaf area index (LAI) were estimated for each tree crown, as they are good indicators to detect *Xf* infections in almond trees (Zarco-Tejada et al., 2021). These leaf and canopy traits were retrieved using pure sunlit tree crown reflectance pixels, obtained from the segmentation method. As this method obtains only plant features from the trees, it prevents artifacts caused by vegetation pixels combined with within-crown shadows, tree boundaries, or from a sunny or shaded soil backdrop that might hinder the quality of the spectra. This procedure was carried out for each specific study site considering the intrinsic variations between each dataset and time of collection (Table 4) described in section 2.2.

A look-up table of 100,000 simulations was created for each dataset by uniformly distributing the parameters shown in Table 4. The rest of the parameters were used in their default ranges. As reflectance is simulated in PRO4SAIL in the 400–2500-nm spectral range with an FWHM of 1 nm, data resampling was carried out to match the spectral resolution of both hyperspectral sensors used in this study. Convolution was performed by applying a Gaussian spectral response function. The inversions of the plant traits derived by model inversion were performed using supported vector machine (SVM) algorithms. SVM models are non-parametric models, based on the statistical learning theory (Vapnik, 1999) and have been widely used in remote sensing studies due to their generalization even when the training dataset is reduced (Mantero et al., 2005), and they showed similar or even better results when compared with more recently proposed algorithms, such as artificial neural

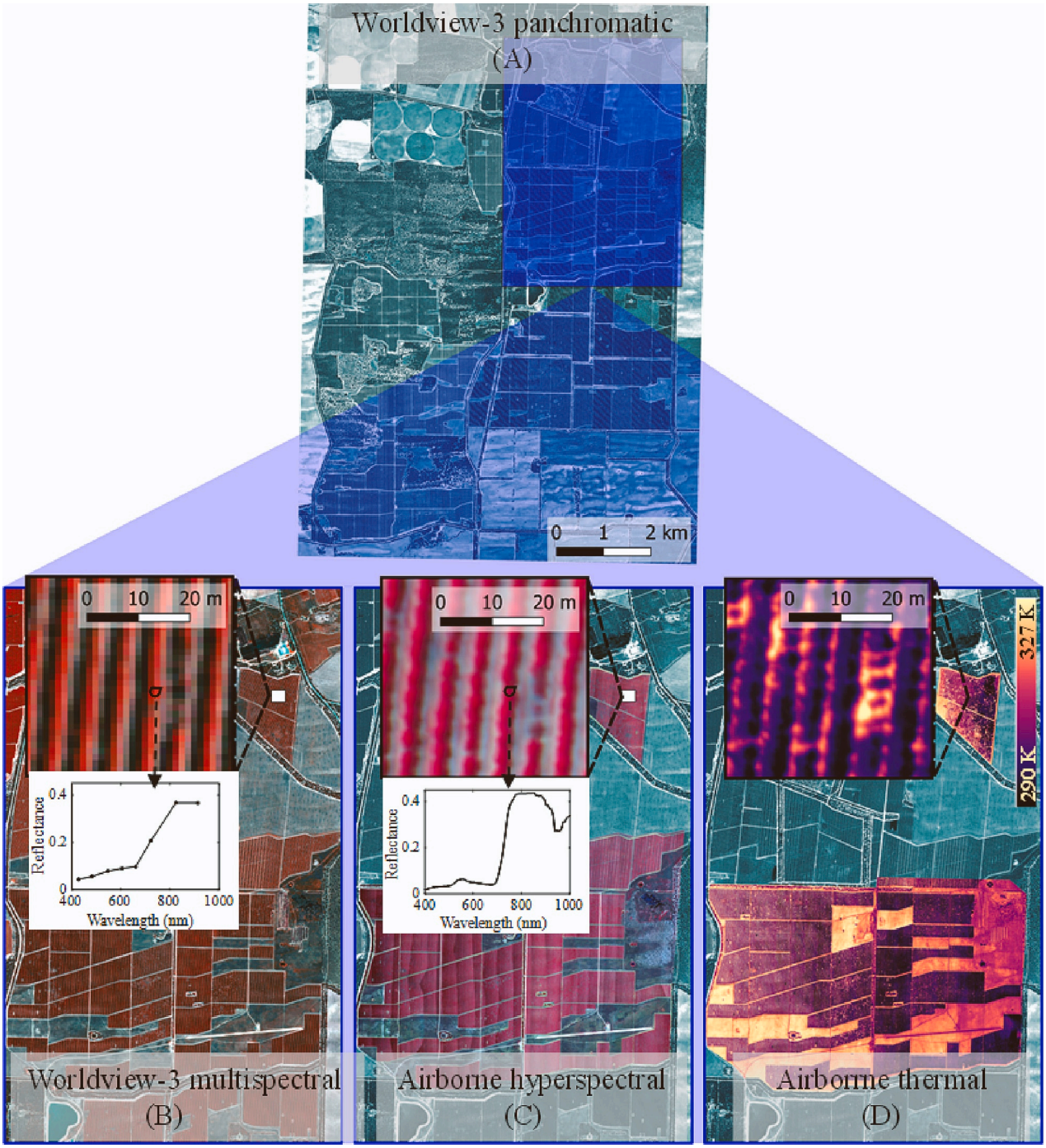

Fig. 2. Comparison of the spatial resolution obtained between the Worldview-3 satellite images and the airborne hyperspectral and thermal imagery. (A) Worldview-3 panchromatic imagery collected in Australia with a pixel size of 0.31 m. (B) Worldview-3 multispectral imagery collected with a pixel size of 1.24 m. (C) Narrow-band hyperspectral imagery collected with a pixel size of 0.29 m. (D) Thermal imagery collected with a pixel size of 0.44 m.

networks (Kuter, 2021; Almendra-Martín et al., 2021). The main purpose of SVM algorithms is to find the hyperplane that maximizes the margin between the classes and to minimize the misclassification error. For regression analyses, this algorithm is named Support Vector Regression (SVR), where the main purpose is to find the function with the maximum deviation between the observed responses for all instances of observation. The so-called kernel technique is used to project a nonlinear problem in a higher dimensional feature space where the problem can be solved by linear solutions. This kernel technique can be applied to both classification and regression problems. For the inversion of the biochemical and structural traits, SVR models were trained in parallel using MATLAB (MATLAB; Statistics and Machine Learning toolbox, parallel computing toolbox and Deep Learning toolbox; Mathworks Inc., Natick, MA, USA), employing as inputs the resampled reflectance and as output the biochemical and structural traits. The SVR algorithms were trained 10-fold using a radial basis function as kernel and optimizing the hyperparameters during training for each variable.

2.5. *Machine learning algorithms to detect Xf and Vd infection and symptom severity in olive and almond trees*

Detection of *Xf*- and *Vd*-induced symptoms was performed for early,

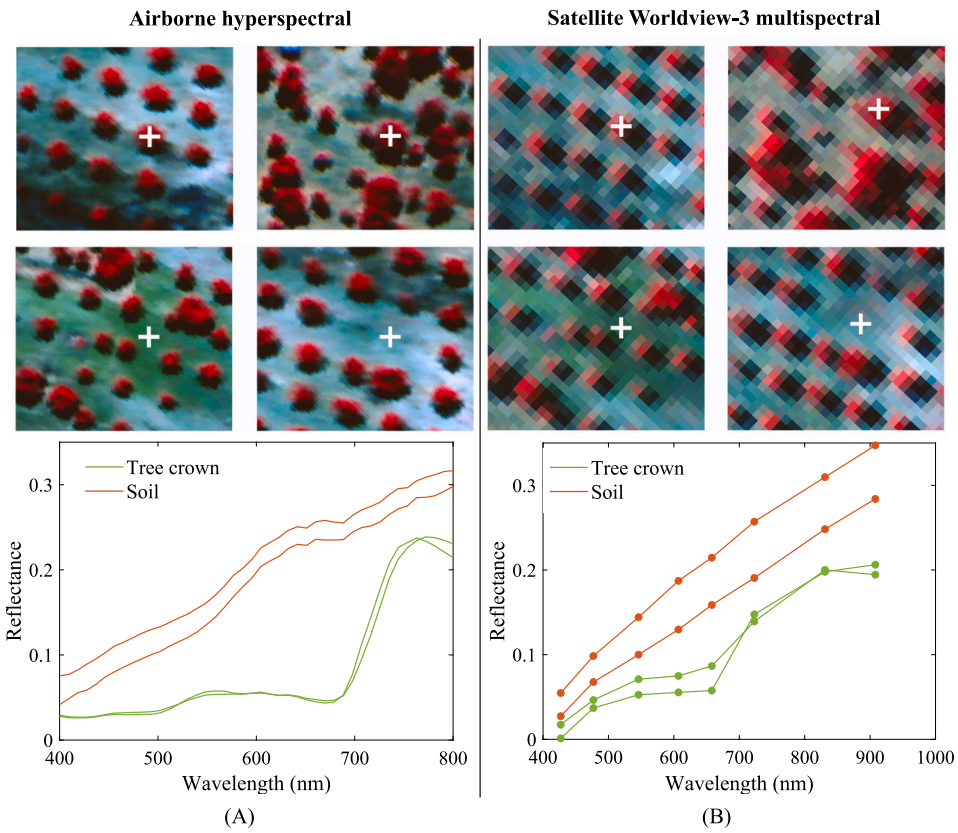

Fig. 3. Comparison of the spectral resolution between narrow-band hyperspectral images and Worldview-3 multispectral images. (A) Calibrated narrow-band hyperspectral imagery showing reflectance spectra for vegetation and soil pixels. (B) Radiometrically calibrated Worldview-3 multispectral images showing reflectance spectra for vegetation and soil pixels.

Table 3
Multispectral indices derived from the Worldview-2 and -3 satellite imagery.

Multispectral indices	Equation	Reference
Ratio vegetation index	$RVI = R_{832.5}/R_{658.8}$	Tucker (1979)
Normalized difference veg. index	$NDVI = (R_{832.5} - R_{658.8})/(R_{832.5} + R_{658.8})$	Rouse et al. (1974)
Green normalized diff. veg. index	$GNDVI = (R_{832.5} - R_{546.2})/(R_{832.5} + R_{546.2})$	Gitelson et al. (2003)
Enhanced vegetation index	$EVI = 2.5 \bullet ((R_{832.5} - R_{658.8})/(R_{832.5} + 6 \bullet R_{658.8} - 7.5 \bullet R_{477.9} + 1))$	Huete et al. (2002)
Enhanced Vegetation Index 2	$EVI_2 = 2.5 \bullet (R_{832.5} - R_{658.8})/(R_{832.5} + 2.5 \bullet R_{658.8} + 1)]$	Jiang et al. (2008)
Wide dynamic range vegetation index	$WDRVI = (0.12 \bullet R_{832.5} - R_{658.8})/(0.12 \bullet R_{832.5} + R_{658.8})$	Gitelson (2004)
Structure Insensitive Pigment Index	$SIPI = (R_{832.5} - R_{477.9})/(R_{832.5} - R_{658.8})$	Peñuelas et al. (1995a, 1995b)
Normalized Ratio Vegetation Index	$NRVI = (RVI - 1)/(RVI + 1)$	Baret and Guyot (1991)
Transformed Vegetation Index	$TVI = \sqrt{[(R_{832.5} - R_{658.8})/(R_{832.5} + R_{658.8}) + 0.5]}$	Deering (1975)
Optimized soil-adjusted veg. index	$OSAVI = (R_{832.5} - R_{658.8})/(R_{832.5} + R_{658.8} + 0.16)$	Rondeaux et al. (1996)
Modified chlorophyll abs. refl. index	$MCARI = [(R_{723.7} - R_{658.8}) - 0.2 \bullet (R_{723.7} - R_{546.2})] \bullet (R_{723.7}/R_{658.8})$	Daughtry et al. (2000)
Transformed chl.abs. refl. index	$TCARI = 3 \bullet [(R_{723.7} - R_{658.8}) - 0.2 \bullet (R_{723.7} - R_{546.2}) \bullet (R_{723.7}/R_{658.8})]$	Haboudane et al. (2002)
MCARI/OSAVI	MCARI/OSAVI	Daughtry et al. (2000)
TCARI/OSAVI	TCARI/OSAVI	Haboudane et al. (2002)
Normalized difference red-edge	$NDRE = (R_{832.5} - R_{723.7})/(R_{832.5} + R_{723.7})$	Gitelson and Merzlyak (1997)
Red-edge chlorophyll index	$RECI = (R_{832.5}/R_{658.8}) - 1$	Gitelson et al. (2005)

middle, and all stages of the disease progression. The trees were classified as asymptomatic (SEV = 0) or at one of three levels of increasing disease severity: i) early stage, which included trees assessed as symptomatic with SEV = 1; ii) middle stage, which included trees assessed as symptomatic with SEV = {1,2}; and iii) all stages, which included all trees assessed as symptomatic (SEV = {1,2,3,4}).

Table 4
Ranges of parameters used to perform simulations with the PRO4SAIL radiative transfer model.

Parameter	Abbreviation	Units	Value / Range
Chlorophyll content	C_{a+b}	[µg/cm^2]	[10,70][a];[10,80][b]; [10,60][c]
Carotenoid content	C_{x+c}	[µg/cm^2]	[0,20][a];[1,20][b];[4,15][c]
Anthocyanin content	Anth.	[µg/cm^2]	[0,7.5][a]; [1,15][b]; [1,18][c]
Dry matter content	Cm	[g/cm^2]	0.012[a,b]; 0.0015[c]
Water content	Cw	[g/cm^2]	0.009[a,b]; 0.001[c]
Mesophyll struct. Coeff.	N	–	[1, 2.5][a];[0.5,3][b,c]
Leaf area index	LAI	[m^2/m^2]	[0.3,5][a]; [1,2.5][b]; [1,3.5][c]
Average leaf angle	LIDF	[deg.]	[0,90][a,b]; [0,90][b]; [40,100][c]
Hot spot parameter	hot	–	0.01[a,b,c]
Observer angle	tto	[deg.]	0[a,b,c]
Sun zenith angle	tts	[deg.]	[0–66.9][a],53.75[b]; 60[c]
Relative azimuth angle	psi	[deg.]	0[a,b,c]

[a] Parameters used for the study sites monitored from 2011 to 2019 in Italy and Spain.
[b] Parameters used for the study sites monitored from 2020 to 2022 in Australia.
[c] Parameters used for the study site monitored in 2021 in Spain.

The classification of SEV = 0 vs. SEV = 1; SEV = 0 vs. SEV ≤2; and SEV = 0 vs. SEV ≥ 1 was performed to i) compare the accuracy of the detection when using as inputs different spatial and spectral resolution data, and ii) assess the progression of the Contribution of the plant traits relevant to detecting each pathogen-induced stress and severity level.

2.5.1. Assessment of the detection of Xf and Vd infection and severity of symptoms

A similar procedure of classifying SEV = 0 (asymptomatic) vs. SEV = 1; SEV = 0 vs. SEV ≤ 2; and SEV = 0 vs. SEV ≥ 1 was performed using different sets of inputs, including i) the PSFT inputs from airborne hyperspectral and thermal images, used as a benchmark when comparing against satellite-derived model performance (these inputs were obtained from previous studies where the classification of 0 vs. all was performed; more details can be found in Zarco-Tejada et al., 2021); ii) hyperspectral-only derived data (C_{a+b}, Anth., C_{x+c}, LAI, LIDF, $SIF_{@760}$, and the non-collinear set of NBHIs) without using the thermal CWSI indicator; iii) reflectance bands from WV-2 and 3 multispectral satellite imagery; and iv) the same inputs as (iii) but including the airborne-derived thermal CWSI indicator. The latter set of inputs was used to assess the importance of obtaining thermal imagery concurrently with Worldview 2 and 3 satellite imagery for improved disease detection. This combination of inputs was assessed because the CWSI is linked to transpiration rates, which are affected by the blockage of water flow through the vascular system of plants infected by these pathogens. Given that thermal infrared satellite sensors have limited spatial resolution, which can hinder early disease detection when relying solely on satellite-derived data, this procedure can be used to assess the need for a multi-sensor approach to enhance the detection of different stages of the disease.

This analysis was carried out to compare the accuracies obtained by training SVM algorithms. These algorithms were trained in parallel with the 10-fold cross-validation procedure. The hyperparameters were optimized using Bayesian optimization during the training step with balance techniques. We used 70% for training and the remaining 30% for testing, and this process was performed 50 times. To evaluate the accuracy of the detection, the overall accuracy (OA) and the *kappa coefficients* (κ) were calculated (Freeman and Moisen, 2008). In addition, the false positive rate (FPR) and false negative rate (FNR) related to sensitivity (the likelihood of properly recognizing true positives while avoiding false negatives) and specificity (the ability to appropriately detect true negatives while avoiding false positives; Trevethan, 2017) were calculated and compared for all datasets.

2.5.2. Contribution of plant traits to detection at progressive stages of Xf and Vd infection and severity

Disease symptoms are expected to affect sensitive plant traits differently over the course of disease. Therefore, we assessed the hyperspectral imagery to evaluate the Contribution of plant traits as a function of the different disease stages (early, middle, and all severity levels). This analysis was performed by training random forest (RF) algorithms for all datasets. RF algorithms were trained using the biochemical and structural traits obtained by model inversion as inputs and adding traits such as CWSI, $SIF_{@760}$, and the non-collinear NBHIs that contributed to the model.

As in Poblete et al. (2021) and Zarco-Tejada et al. (2021), C_{a+b}, Anth., C_{x+c}, LAI, LIDF, CWSI, and $SIF_{@760}$ were inputs into RF models since they are directly related to the plant physiological status. First, the dimensionality of the NBHI pool of indices was reduced by the variance inflation factor (VIF) analysis (James et al., 2013), where indices from the NBHI pool with a VIF > 5 (Akinwande et al., 2015) were removed. Then, a recursive feature elimination approach was performed by classifying asymptomatic (SEV = 0) vs. all disease severity levels (SEV ≥ 1), and those indices that did not improve the classification accuracies (OA) and the *kappa coefficients* (κ) were not included in the models. Indices retained in this step were included in the rest of the detection analyses for the early and middle stages of the disease progression. A balanced dataset of both asymptomatic and symptomatic trees was randomly chosen from 80% of the trees to determine the Contribution of plant traits in the detection. RF models were then trained using the balanced dataset of symptomatic/asymptomatic trees, and the importance of each predictor was determined using the permutation of the out-of-bag method (Thomas et al., 2021). As all the plant traits and indices used have already being reported as relevant to detect these diseases at all stages of infection, the progression assessment of their Contribution was performed to assess the role they play for the detection of the different stages of disease progression. This analysis will allow to link this dynamics with the progressive physiological changes as a function of disease severity. The hyperparameters of the models were optimized using a Bayesian optimization method in MATLAB (Statistics and Machine Learning toolbox; MathWorks Inc., Natick, MA, USA). After assessing the progression of the contributions for each plant trait, we compared the predictions obtained by the hyperspectral-only derived data with the satellite-only data. We used the datasets from Australia to study *Vd* infections affecting olive trees, which were monitored during two consecutive years. We first predicted asymptomatic and infected symptomatic (irrespective of the severity level) olive trees at a plot level monitored in the 2020 campaign. Then, considering that in the 2021 season a larger area and a larger number of trees were assessed, we validated our results with the second-year campaign by comparing the percentage of incidence of disease predicted by both the airborne hyperspectral and the satellite sources. Following this, we investigated those orchards with major discrepancies between both sources by contrasting their predictions against the visual assessments performed in the second year.

As the hyperspectral-derived plant traits gave valuable physiological information that could not be retrieved by the available satellite-only information, we investigated whether this discrepancy was produced by the inability of the satellite-derived models to capture symptoms triggered in trees at the early stages of disease progression. We compared the absolute differences of the percentage of trees predicted as symptomatic (SEV ≥ 1) with the proportion of trees evaluated as early-stage (SEV = 1) in the second year to assess if the major differences were associated with a higher proportion of trees at early stages.

3. Results

The indices calculated from both hyperspectral and Worldview multispectral satellite data showed consistent trends as a function of all levels of disease severity (Supplementary Fig. 1). The indices related to canopy structure, e.g. NDVI (Rouse et al., 1974), EVI (Huete et al., 2002), and OSAVI (Rondeaux et al., 1996) decreased when the severity increased (Supplementary Fig. 1A, 1B and 1G, respectively). In addition, chlorophyll-related indices such as TCARI (Haboudane et al., 2002), MCARI (Daughtry et al., 2000), and the ratio TCARI/OSAVI (Haboudane et al., 2002) (Supplementary Fig. 1E, 1F and 1H, respectively) also showed a decrease as a function of severity.

3.1. Detection accuracy of Xf infections in olive and almond trees

The detection of *Xf* infections in olive trees using only the Worldview satellite multispectral data showed OAs of 0.62 and 0.61, κ values of 0.29 and 0.22, FNRs of 0.44 and 0.51, and FPRs of 0.43 and 0.43, for middle and early stages of the disease progression, respectively (Fig. 4A and 5A). These results improved when adding the thermal CWSI indicator, showing OAs of 0.67 and 0.63, κ values of 0.35 and 0.26, FNRs of 0.35 and 0.34, and FPRs of 0.31 and 0.38, respectively. The same behavior was observed when detecting symptomatic trees at any level of infection, where the accuracies were higher when the CWSI indicator was added (OAs from 0.63 to 0.7, κ values from 0.29 to 0.39, FNRs from 0.41 to 0.34, and FPRs from 0.38 to 0.25).

The results using satellite-derived data were considerably lower compared to the PSFT benchmark dataset for the detection of early, middle, and all stages of the disease progression. The highest accuracy was reached by the PSFT dataset for all stages of the disease progression, with an OA of 0.79, a κ of 0.46, FNR = 0.32, and an FPR = 0.2. When detecting middle and early stages, the OA values were 0.71 and 0.65, κ was 0.41 and 0.29, FNR was 0.34 and 0.35, and FPR was 0.24 and 0.38, respectively. The use of hyperspectral-derived data without the thermal CWSI indicator slightly underperformed the PSFT dataset with OA = 0.71, κ = 0.41, FNR = 0.34, and FPR = 0.25, for the detection of all stages. For the middle and early stages, the accuracies obtained were OA = 0.68–0.64, κ = 0.27–0.36, FPR = 0.29–0.39, respectively, and FNR = 0.35 for both cases. The detection of *Xf* effects on almond trees using only the Worldview data yielded the poorest performance for all cases. However, when detecting middle and all stages of *Xf* disease progression, the performance of Worldview imagery improved when the thermal-based CWSI was added in the model. The OA increased from 0.74 to 0.77 and from 0.81 to 0.84, respectively. The κ increased from 0.49 to 0.55 and from 0.63 to 0.67 (Fig. 4B). The FNRs decreased from 0.24 to 0.23 and from 0.24 to 0.17 for middle and all-stage detection. In the case of the FPR, they remained stable at 0.18 and 0.12 in both cases (Fig. 5B). Nevertheless, for the detection of the early stages of the *Xf* disease progression, the inclusion of CWSI had almost no effect, with OA = 0.74 for both cases, and the κ, FNR, and FPR varying from 0.47 to 0.49, 0.35 to 0.3, and 0.25 to 0.23, respectively. As in *Xf*/olive, in *Xf*/almond the PSFT was the best performing in all cases and compared with the satellite-derived data only, a major improvement was observed for middle and early stages. The accuracies at early stages varied from OA = 0.74 to 0.79 (κ from 0.47 to 0.6); for middle stages from OA = 0.74 to 0.85 (κ from 0.49 to 0.71); and all stages from OA = 0.81 to 0.91 (κ from 0.63 to 0.81). The use of hyperspectral-derived data only compared with the PSFT dataset showed a slight difference in accuracy, with an average of 0.1 units of difference for both OA and κ.

3.2. Detection accuracy of Vd infections in olive trees

As in the assessment of *Xf*, adding CWSI to the satellite data improved the detection of *Vd* infections in olive trees. For the early stages of disease progression, OA improved from 0.72 to 0.78 and *k* from 0.45 to 0.56 (Fig. 4C). For the middle stages of disease progression, OA increased from 0.76 to 0.85 and *k* from 0.54 to 0.71, and for all stages of disease progression, the improvement was from OA = 0.83 to 0.86 and *k* = 0.68 to 0.72. The improved accuracy obtained when adding the CWSI to the multispectral satellite data highlights the need for high-resolution thermal imagery to detect both infections; however, it is not feasible to obtain such resolution using conventional satellite platforms.

The PSFT dataset contributed the most to the prediction compared with using the satellite-only derived data, principally with a major effect on the detection of early and middle stages. When detecting early stages, the OA was improved from 0.72 to 0.85, the κ increased from 0.45 to 0.69, the FNR decreased from 0.27 to 0.12, and the FPR from 0.32 to 0.11. For the detection of middle stages, OA increased from 0.76 to 0.9, while *k* increased from 0.54 to 0.79. The FNR was reduced from 0.26 to 0.12 and the FPR from 0.23 to 0.09, while for all stages the OA increased from 0.83 to 0.92, the *k* increased from 0.68 to 0.83, and the FNR and the FPR decreased from 0.21 to 0.08 and from 0.14 to 0.07, respectively.

3.3. Progression of plant traits to detect early, middle and all stages of Xf and Vd infections

We further studied the lower performance of the multispectral satellite data compared to airborne hyperspectral data for the early detection of both diseases. The significant improvement observed with the PSFT dataset compared to the use of satellite-only data allowed us to evaluate the plant traits sensitive to early levels of infection, with regard to their influence on the detection of early stages. First, we evaluated the distribution of the plant traits previously identified as sensitive to infection and useful for detection (Zarco-Tejada et al., 2021), comparing them for the early, middle, and all stages of the disease progression with the asymptomatic trees. As a Dunnett's test showed that the relevant plant traits (i.e., CWSI, PRI_n, $SIF_{@760}$, C_{a+b}, Anth., and LAI) were statistically different when comparing all stages of disease progression with the asymptomatic trees (Supplementary Fig. 2), we then assessed the progressive contributions (importance) of the most sensitive plant traits. NPQI had the greatest Contribution to the detection of *Xf* in both tree species for middle and all stages of disease progression (as in Zarco-Tejada et al., 2018, 2021), showing an importance of 0.22 and 0.20 for olive, respectively (Fig. 6A), and 0.21 and 0.22 for almond, respectively (Fig. 6B). At the earliest stages, PRI_n made the largest Contribution when detecting symptoms affecting almond trees, with an importance of 0.25, while for olive, NPQI again had the greatest Contribution, at 0.23. PRI_n showed the best separability among severity levels of disease progression, with differences of 0.04, 0.22, 0.26, and 0.48 between asymptomatic and early, middle, and advanced stages. On the other hand, LAI showed the lowest differences between these groups with 0.03, 0.07, 0.1, and 0.05, respectively (Supplementary Fig. 2).

The importance of CWSI was higher when detecting *Xf*-infected olive trees compared to its Contribution in almonds, but in the latter it increased as the stages included more advanced symptoms of infection. For the detection of *Vd*-infected olive trees, CWSI had a lower contribution when detecting early stages of infection characterized by low severity levels (being the sixth-ranked most important plant trait with an importance of 0.08). Nevertheless, it increased with more advanced stages of disease progression, ultimately being the most important factor for detecting disease incidence, with an importance of approximately 0.19 (Fig. 6C). In the same case (*Vd*/olive), the Contribution of NPQI was low and remained stable when adding trees with higher severity in the classification (with a mean importance of 0.06 in the three stages), which could indicate that NPQI has greater specificity for detection of *Xf* infections. The Contribution of PRI_n was the highest for the detection of early stages of *Vd* infection in olive trees, and it decreased as a function of the disease severity (from 0.24 down to 0.15). Notably, C_{x+c}, LIDF, and $SIF_{@760}$ showed almost no changes when comparing their Contribution to the detection of middle and early stages of disease development. The anthocyanin content was highly relevant in the detection of *Xf*/olive at all stages, increasing from 0.02 up to 0.15 compared with

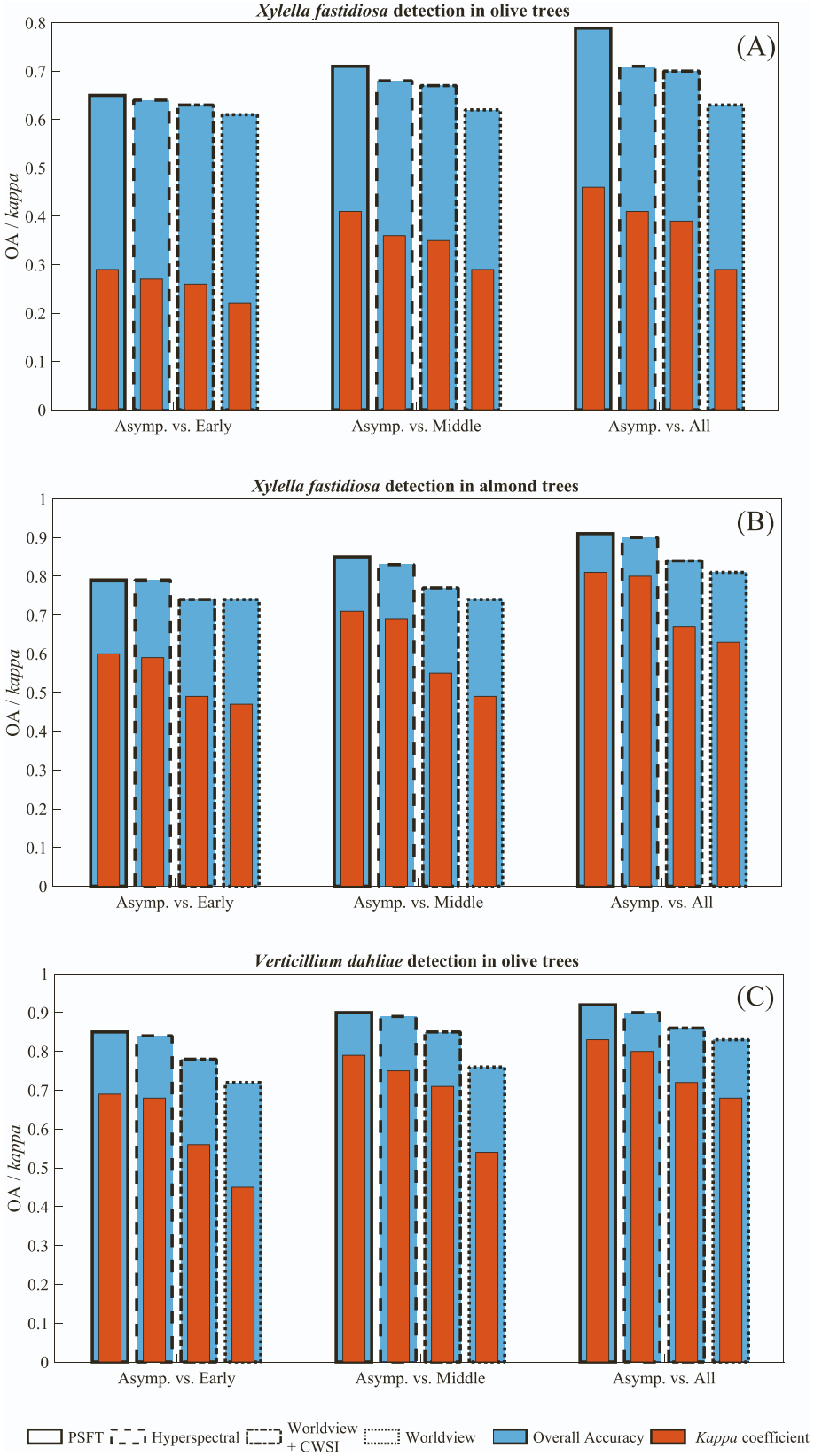

Fig. 4. Comparison of the accuracies obtained at a multi-spatial and -spectral resolution for the detection of *Xylella fastidiosa* (*Xf*) and *Verticillium dahliae* (*Vd*) infections at early, middle, and all stages of disease progression. (A) Accuracy of the detection of *Xf* infections in olive trees. (B) Accuracy of the detection of *Xf* infections in almond trees. (C) Accuracy of the detection of *Vd* infections in olive trees monitored during 2020–2022.

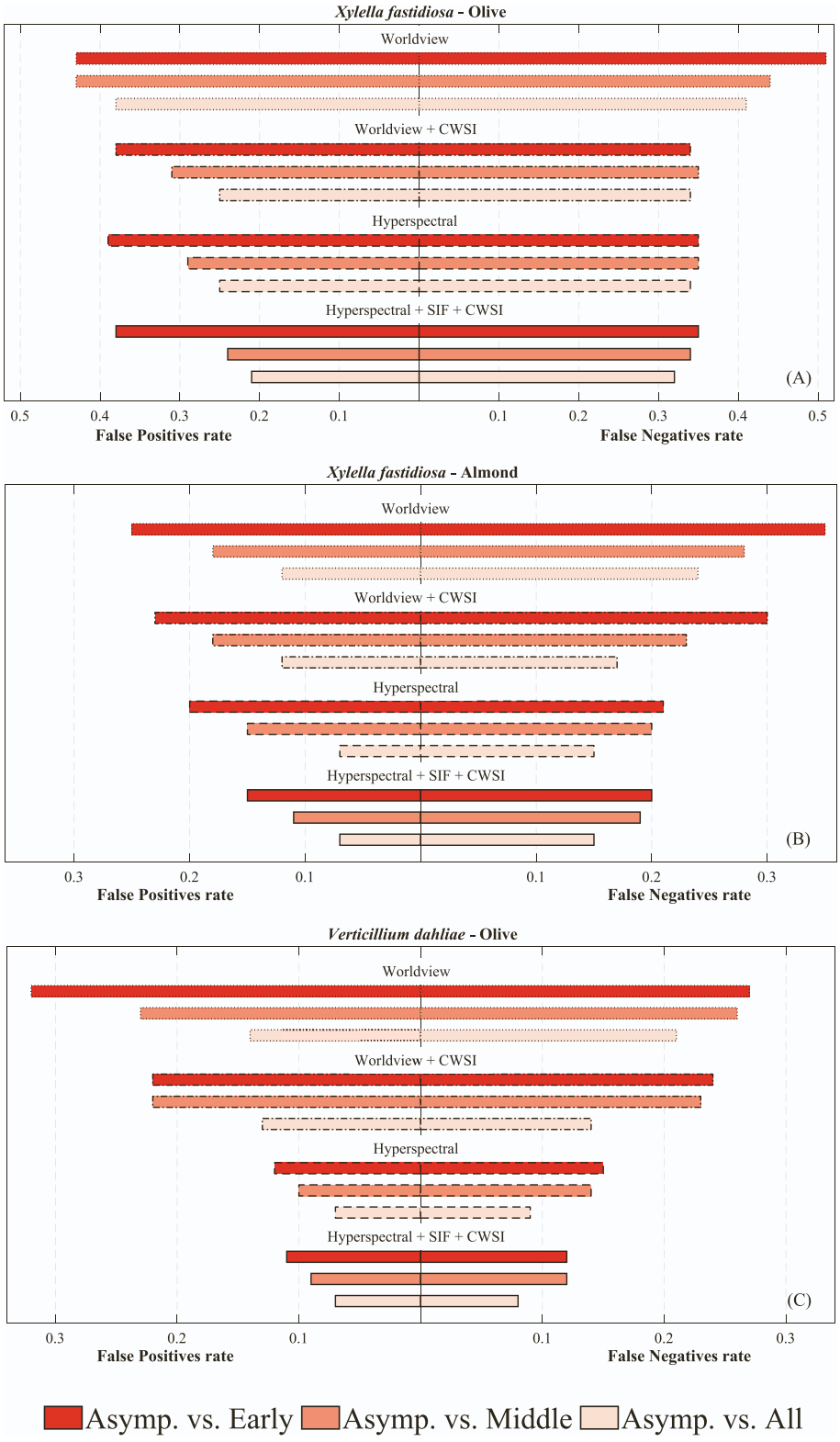

Fig. 5. Comparison of the false positive rate (FPR) and false negative rate (FNR) obtained at a multi-spatial and -spectral resolution for the detection of *Xylella fastidiosa* (*Xf*) and *Verticillium dahliae* (*Vd*) infections at early, middle, and all stages. (A) FPR and FNR obtained for the detection of *Xf* infections in olive trees. (B) FPR and FNR obtained for the detection of *Xf* infections in almond trees. (C) FPR and FNR obtained for the detection of *Vd* infections in olive trees monitored in 2020–2022.

early stages, while for the rest of the cases it remained relatively low compared with the other plant traits.

3.4. Assessment of the predictive capabilities of airborne hyperspectral and satellite multispectral imagery for detecting Xf and Vd infections

The overall accuracies achieved when using the PSFT dataset

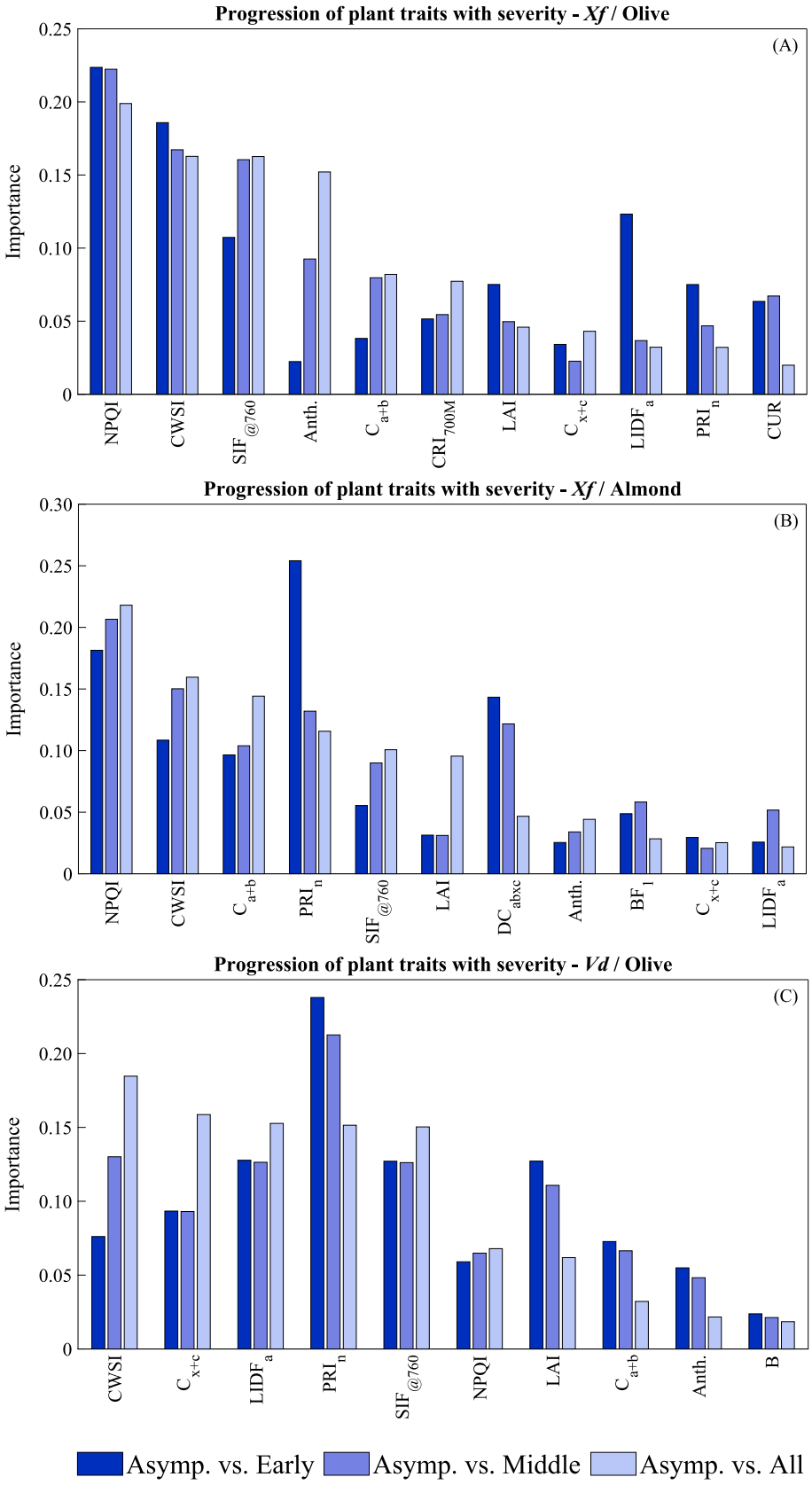

Fig. 6. Progressive Contribution of the most sensitive plant traits to detection of *Xylella fastidiosa* (*Xf*) and *Verticillium dahliae* (*Vd*) in olive and almond trees at early, middle, and all stages of disease progression. Progression of the plant trait contributions to detect *Xf* in olive trees (A), *Xf* in almond trees (B), and *Vd* in olive trees (C).

compared to the hyperspectral-only dataset were not severely compromised, showing on average differences of 0.025 for all stages of disease progression, 0.028 for intermediate stages of disease progression, and 0.01 for early stages. Based on this, we performed a tree-based prediction over a large area to detect *Vd*-infected olive trees (Fig. 7). We applied the models to airborne hyperspectral and satellite multispectral images to compare the spatial variability of the resulting predictions, evaluating the areas where the larger errors were obtained.

The areas predicted as infected by the models built with hyperspectral data were larger compared with the areas predicted by the satellite (Fig. 8). When assessing the errors obtained by both datasets at the plot level, results yielded $R^2 = 0.54$ and RMSE = 0.3.

The proportion of infected trees detected as being symptomatic (all disease severity levels) was higher when using the airborne hyperspectral data than when using satellite data; the predictions for some orchards were highly inaccurate, while others were accurate. To determine the cause of inaccuracies in disease detection using satellite data, we evaluated the frequency of visual assessments for each severity level in orchards that yielded the least accurate and most accurate predictions (Fig. 9). For the plots where the discrepancy between satellite-based predictions and the hyperspectral-based predictions was the highest (Fig. 9a-c), the proportion of trees at low severity levels was higher for all cases, whereas trees at advanced stages (SEV = 4) were not observed. By contrast, orchards with the lowest discrepancies (Fig. 9d-f) had the smallest proportion of trees at the early stages of disease progression and the highest proportion of trees at advanced stages. This analysis indicated that the major discrepancies between satellite data and airborne hyperspectral data were generally observed for trees at the early stages of disease progression, while the greatest similarity was obtained when a greater proportion of the trees were at advanced stages and fewer (or none) at early stages of progression. To further illustrate this point, as shown in Fig. 10, we assessed the relationship between the differences in the frequency of symptomatic trees detected between the satellite and airborne hyperspectral data compared to the proportion of trees at the early stages of disease progression.

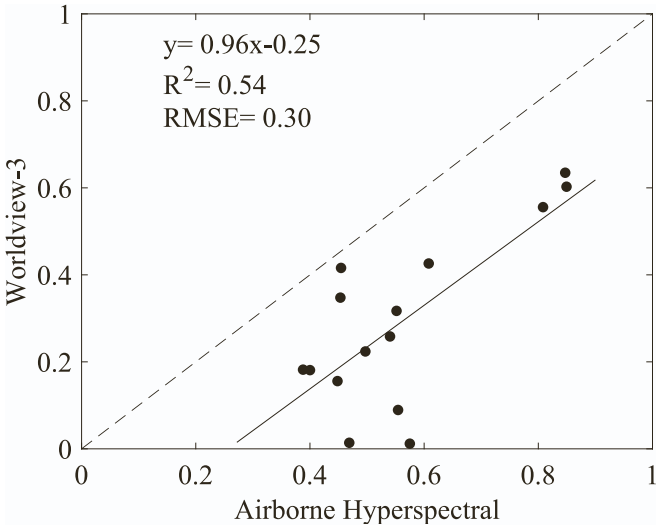

Fig. 8. Relationship between the proportion of olive trees predicted as *Verticillium dahliae*- symptomatic (all disease severity levels) using only hyperspectral-derived information with the proportion of trees predicted as symptomatic using only the satellite multispectral information.

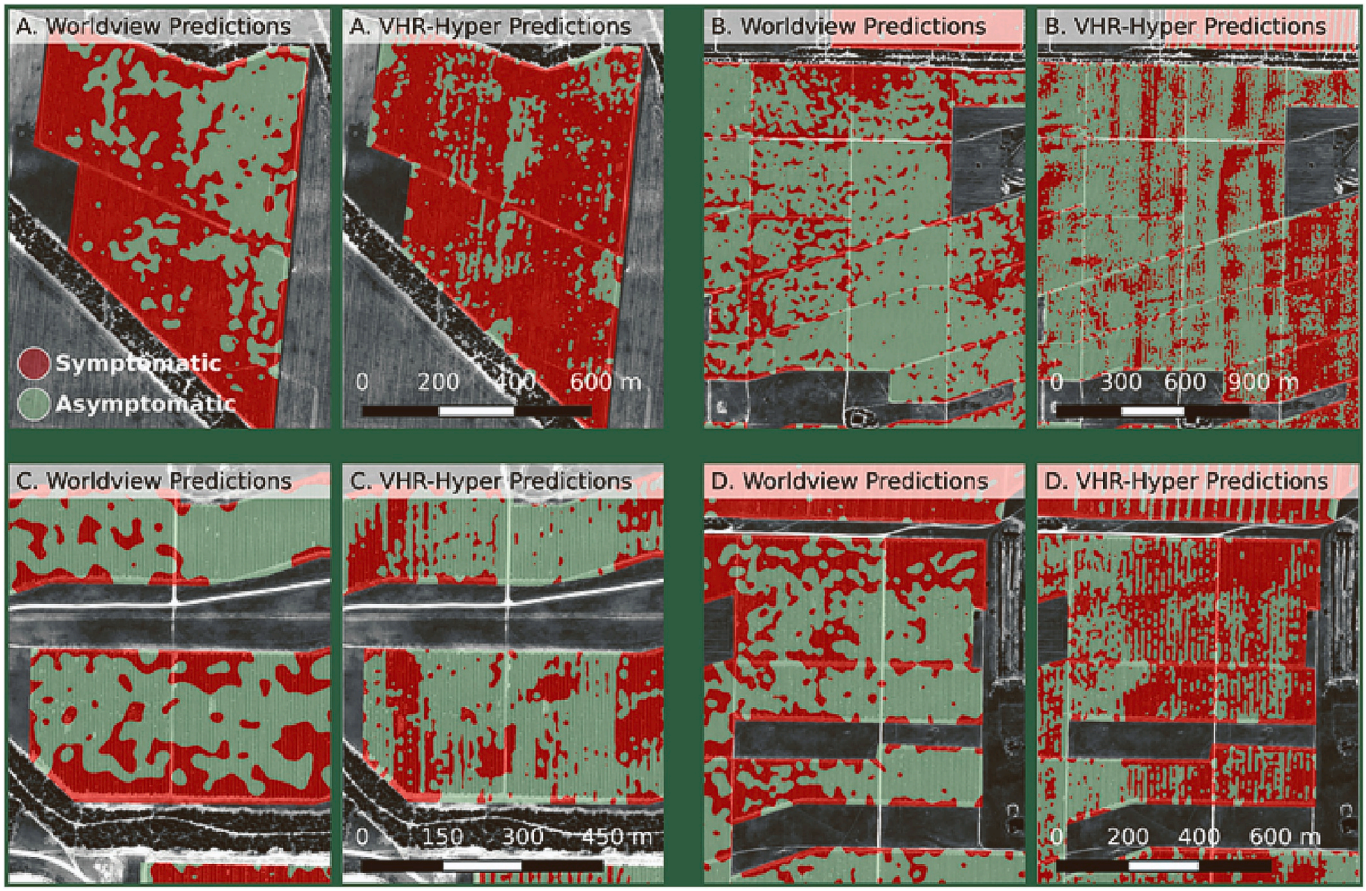

Fig. 7. Spatial variability of tree-based prediction to detect asymptomatic and *Verticillium dahliae*-symptomatic olive trees. Predictions using the model built with only hyperspectral-derived information (right panels) or the model built using only satellite multispectral information (left panels).

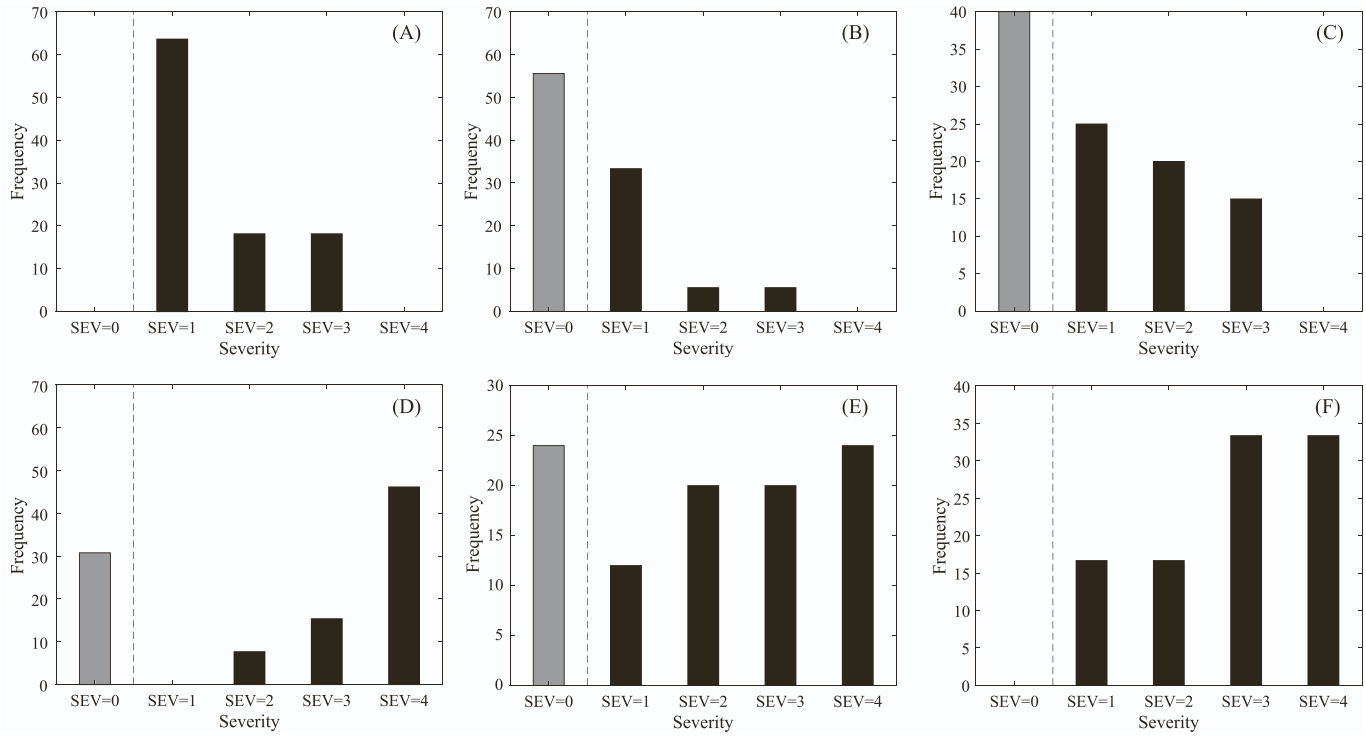

Fig. 9. Distribution of the visual assessment results in the plots with the highest (A-C) and lowest (D—F) discrepancies between the predictions obtained from the model built using only the hyperspectral data and the model built using only the satellite multispectral data for *Verticillium dahliae*–affected orchards.

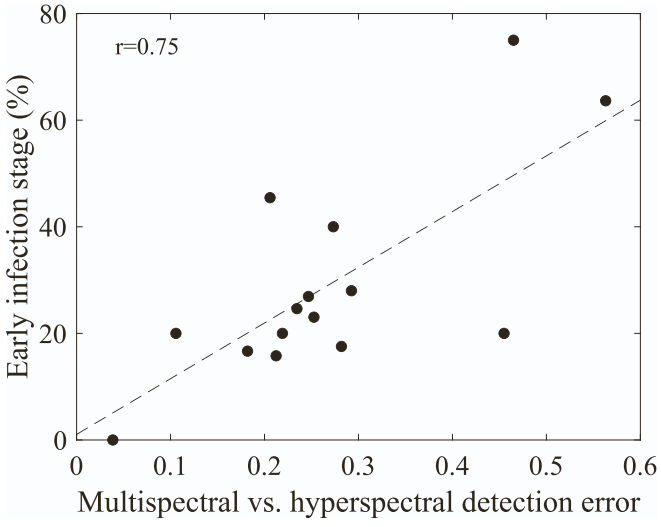

Fig. 10. The percentages of early-stage infected trees (SEV = 1) detected in the visual assessments relative to the differences in infected trees detected by the model built using only the hyperspectral data and the model built using only the satellite multispectral data for *Verticillium dahliae*–affected orchards.

A positive relationship was observed between the error of symptomatic trees detected by satellite and airborne hyperspectral data, compared with the proportion of trees at the early infection stage. This suggests that the percentage of trees at an early stage of disease progression was the main driver of the inaccuracies obtained by the models built with satellite data rather than only an impact of the spatial resolution. This observation is supported by the finding that plots with the smallest errors had no trees showing low severity levels, which typically correspond to early stages of disease progression.

4. Discussion

4.1. Impact of spectral resolution on the detection of infected trees

Remote sensing methods at various spectral and spatial resolutions have been proposed for large-scale detection of harmful pests and pathogens affecting agriculture (Zarco-Tejada et al., 2018 and 2021, El-Ghany et al., 2020). Several studies have assessed the role that spectral resolution plays in the accuracy of the detection for different diseases (Mewes et al., 2011; Poblete et al., 2020; Bendel et al., 2020). For example, the study by Poblete et al. (2020) suggested that the benchmark was the best-performing dataset compared with a reduced simulated bandset coupled with the thermal indicators CWSI and SIF. They found that the accuracies using PSFT decreased from 80% ($k = 0.42$) to 74% ($k = 0.36$), compared to when using the optimally reduced bandset consisting of six bands (centered at 400, 669, 760, 714, 423, and 525 nm with a FWHM of 10 nm) including the CWSI. They also demonstrated that the bandsets simulating the conventional RGB (red, green, and blue) and CIR (near-infrared, green, and red) sensors were the worst performing ones with OA = 66.7% and 63% and $k = 0.25$ and 0.17, respectively. This is also in line with the findings of Bendel et al. (2020), who used ground-based hyperspectral and UAV multispectral images to identify the grapevine trunk disease Esca in vineyards. When using VNIR hyperspectral (400–1000 nm) information, the accuracies were 73% and 81% for the prediction over two consecutive years, and when using lower spectral resolutions, it decreased to 60% and 58% for the detection of infected vines showing 25–50% of symptoms.

Mewes et al. (2011) successfully detected *Blumeria graminis* infections of wheat cultivars using HyMap imagery. Surprisingly, using only 13 bands, the authors obtained similar results to those obtained using 109 bands after a feature selection process ($k = 0.59$ and 0.57, respectively). Nevertheless, they did not compare the accuracies of their results with those obtained using physiological-related plant traits derived from hyperspectral data, which we have shown to be critical for detecting early stages of infection. In the present study, results were not highly compromised using the hyperspectral-derived information

compared with the PSFT. However, the accuracy of the detection underperformed when using multispectral satellite images. For early stages of disease progression, the highest accuracy was OA = 0.84 and κ = 0.68 when detecting *Vd* infections in olive trees using the hyperspectral-derived dataset, while the accuracy was OA = 0.72 and κ = 0.45 (and a minimum of OA = 0.61 and κ = 0.22 for the *Xf*-olive dataset) using the multispectral-derived dataset. The hyperspectral-derived plant traits provide valuable physiological information that could not be retrieved with satellite-only information and contributed more as a function of disease severity. This was consistent with our findings, which suggested that the model built with satellite-only data showed more errors when the prediction was performed on plots comprising trees at the early stages of disease development.

In comparison to the PSFT dataset, detecting infections using solely hyperspectral-derived indicators without adding CWSI resulted in lower prediction accuracy for all disease severity levels. Notably, the addition of the CWSI had a lower influence on the detection of early stages of disease. Both of these xylem-invading pathogens gradually reduce water flow through the xylem, lowering transpiration rates (Ribeiro et al., 2003). As the decrease in the transpiration rates is directly connected to an increase in CWSI (Idso et al., 1981) and it does not occur at the early stages of infection (López-Escudero and Mercado-Blanco, 2011), the contribution of CWSI is likely accentuated at more advanced stages of disease progression when a higher proportion of the canopy showing visible symptoms is included in the classification.

4.2. Impact of spatial resolution on the detection of infected trees

High-resolution hyperspectral and thermal images have been successfully used to detect xylem-limiting pathogens and differentiate disease from confounding symptoms due to water stress (Zarco-Tejada et al., 2021). However, the operational use of high-resolution commercial satellites for the detection of these vascular diseases has needed further assessment. The detection of infections and pests could be enhanced by using satellite images with higher spatial resolution, i.e., GeoEye-1, Pleiades, WorldView-3 and -4, and GaoJing-1, rather than low-resolution satellite platforms such as Landsat (Yang, 2020). In this regard, Santoso et al. (2019) implemented a machine learning algorithm using WV-3 images to detect basal stem rot disease severity in oil palm plantations using SVM, RF, and decision trees. Despite the low accuracies obtained in their study (OA ~ 0.53 and κ ~ 0.35), they determined that SVM and RF were the most accurate models to predict the disease, which is consistent with the models implemented in our study. Li et al. (2015) detected Huanglongbing (HLB) disease caused by a phloem-limited bacterium *Candidatus Liberibacter* asiaticus using WV-2 imagery, with accuracies of 81% and κ = 0.46. In their study, the addition of thermal CWSI was not assessed, and it could play a key role in the detection since HLB can trigger symptoms that can be confounded by starch allocation and/or nutrient deficiency responses (Cimo et al., 2013).

In the current study, adding airborne CWSI to the satellite data improved the disease detection accuracy by 10–15% and increased the κ coefficient by >0.2 units. This improvement has practical implications, especially given the need for high-resolution thermal images to derive thermal indicators such as CWSI from pure vegetation pixels. Thermal infrared satellite sensors provide low spatial resolution (Tomlinson et al., 2011), which restricts the ability to detect plants at the early stages of disease progression using only satellite-derived data. Thus, a multi-sensor approach combining satellite and airborne platforms is key for in-depth stress detection (Berger et al., 2022), especially for detection of the initial stages of infection. Previous studies focused on the detection of *Xf* and *Vd* infections using lower resolution satellite imagery, such as in Hornero et al. (2020), have made great progress in assessing the evolution of symptoms caused by *Xf* using Sentinel-2 data from two consecutive years collected with a spatial resolution of 20 m and 60 m. They showed that the ARVI and OSAVI indices had better performance in tracking disease incidence and severity progression. Nevertheless, the analysis of the ability of high-resolution multispectral satellite imagery to detect early, middle, and advanced stages of the disease compared with hyperspectral data could not be performed. In our study we evaluated various stages of disease progression using a spatial resolution of 1.84 and 1.24 m. The results demonstrated that, in all cases, the PSFT benchmark dataset (Zarco-Tejada et al., 2018 and 2021) outperformed the models using multispectral satellite-derived data in detecting early, middle, and advanced stages of disease progression.

When working with low and medium spatial resolution satellite imagery, a major challenge is to properly separate the spectral signal of vegetation from the mixed signals of soil background and understory vegetation. Previous research has used medium- and low-spatial resolution satellite data, such as that obtained using Sentinel-2, to detect symptoms induced by *Xylella fastidiosa* and *Verticillium dahliae*. However, the accuracy of plant trait quantification for disease identification is limited by the effect of soil background on pure vegetation reflectance, which varies with the spatial resolution of the image. By contrast, high spatial resolution imagery from Worldview 2 and 3 is more effective at distinguishing green vegetation from soil background responses and acquiring precise soil pixel data compared to coarser resolution imagery (Fernández-Guisuraga et al., 2020; Fernández-Guisuraga et al., 2021). The current findings were consistent across reflectance spectra and indices obtained from airborne hyperspectral and Worldview multispectral imagery and showed a trend in relation to disease severity (see Supplementary Fig. 1). However, it should be noted that our study was conducted across multiple sites and dates, and soil background effects can have different impacts on the spectral data obtained from higher resolution satellite data. We demonstrated that the main factor contributing to inaccuracies in disease detection was the percentage of trees at an early stage of disease progression rather than the impact of low spatial resolution. Nonetheless, a subsequent simulation study will be conducted to evaluate the effects of spatial resolution on the detection of *Xf* and *Vd* infections, particularly in discontinuous tree orchards and in non-homogeneous crops.

5. Conclusions

We compared high-resolution multispectral WV-2 and -3 imagery against a high-resolution hyperspectral and thermal dataset (PSFT benchmark dataset) in terms of their accuracy in detection of vascular diseases in almond and olives trees due to *Xylella fastidiosa* (*Xf*) and *Verticillium dahliae* (*Vd*) pathogens. WV-2 and -3 satellite data successfully detected disease incidence, yielding OA = 0.63–0.83 and κ = 0.29–0.68. Nevertheless, the early stages of disease progression were associated with poorer results from the satellite data (reducing κ to 0.3–0.69) due to the lack of suitable spectral bands for detection at that stage, such as the bandsets needed for calculating the blue NPQI index, solar-induced-fluorescence SIF, PRI_n, and anthocyanins. Given the vascular nature of the pathogens studied here and the fact that water stress is one of the main symptoms caused by both pathogens, the addition of thermal information in the form of the CWSI water stress trait to the satellite data improved the prediction by 10–15% and by >0.2 in the κ coefficient for both the satellite and aerial platforms. Overall, this study demonstrates that the detection of intermediate and advanced disease due to *Xf* and *Vd* vascular pathogens can be successfully carried out with commercial multispectral Worldview imagery, while the early detection of the symptoms requires hyperspectral data.

Credit author statement

T.P., and P.J.Z.-T. designed the objectives of this study and designed research; P.J.Z.-T supervised the work; J.A.N.-C. A.H., C.C., R.C., and B. B.L. carried out field work and airborne data collections; T.P. analysed data, performed research and wrote the paper, and J.A.N.-C., A.H., C.C.,

R.C., R.H.-C., B.B.L. and P.J.Z.-T. contributed and provided comments. All authors read and approved the final submission.

Declaration of Competing Interest

The authors declare that they have no known competing financial interests or personal relationships that could have appeared to influence the work reported in this paper.

Data availability

Data will be made available on request.

Acknowledgements

We thank QuantaLab-IAS-CSIC staff members A. Vera, D. Notario, and R. Romero for laboratory assistance, and M. Saponari, D. Boscia, M. Morelli, L. Susca, M. Montes-Borrego, M. Romás-Écija, G. Leon, J.L. Trapero-Casas and D. Sacristán for their strong support during the field campaigns. The study was partially funded by the European Union's Horizon 2020 Research and Innovation Programme through grant agreements POnTE (635646) and XF-ACTORS (727987), as well as by projects AGL2009-13105 from the Spanish Ministry of Education and Science, P08-AGR-03528 and P18-RT-4184 from the Regional Government of Andalusia and the European Social Fund, project E-RTA2017-00004-02 from "Programa Estatal de I+D+I Orientada a los Retos de la Sociedad" of Spain and FEDER, Intramural Project 201840E111 from CSIC and ITS2017-095: Design and Implementation of control strategies for *Xylella fastidiosa*, Project 5. Government of the Balearic Islands, Spain. The views expressed are purely those of the writers and may not in any circumstance be regarded as stating an official position of the European Commission.

Appendix A. Supplementary data

Supplementary data to this article can be found online at https://doi.org/10.1016/j.rse.2023.113698.

References

Akinwande, M.O., Dikko, H.G., Samson, A., 2015. Variance inflation factor: as a condition for the inclusion of suppressor variable (s) in regression analysis. Open J. Stat. 5 (07), 754.

Almendra-Martín, L., Martínez-Fernández, J., Piles, M., González-Zamora, Á., 2021. Comparison of gap-filling techniques applied to the CCI soil moisture database in southern Europe. Remote Sens. Environ. 258, 112377.

Bannari, A., Morin, D., Bonn, F., Huete, A., 1995. A review of vegetation indices. Remote Sens. Rev. 13 (1–2), 95–120.

Baret, F., Guyot, G., 1991. Potentials and limits of vegetation indices for LAI and APAR assessment. Remote Sens. Environ. 35 (2–3), 161–173.

Barnes, J.D., Balaguer, L., Manrique, E., Elvira, S., Davison, A.W., 1992. A reappraisal of the use of DMSO for the extraction and determination of chlorophylls a and b in lichens and higher plants. Environ. Exp. Bot. 32 (2), 85–100.

Bendel, N., Kicherer, A., Backhaus, A., Klück, H.C., Seiffert, U., Fischer, M., Voegele, R.T., Töpfer, R., 2020. Evaluating the suitability of hyper-and multispectral imaging to detect foliar symptoms of the grapevine trunk disease esca in vineyards. Plant Methods 16 (1), 1–18.

Berger, K., Machwitz, M., Kycko, M., Kefauver, S.C., Van Wittenberghe, S., Gerhards, M., Verrelst, J., Atzberger, C., van der Tol, C., Damm, A., Rascher, U., Herrmann, I., Paz, V.S., Fahrner, S., Pieruschka, R., Prikaziuk, E., Buchaillot, M.L., Halabuk, A., Celesti, M., Koren, G., Gormus, E.T., Rossini, M., Foerster, M., Siegmann, B., Abdelbaki, A., Tagliabue, G., Hank, T., Darvishzadeh, R., Aasen, H., Garcia, M., Pôças, I., Bandopadhyay, S., Sulis, M., Tomelleri, E., Rozenstein, O., Filchev, L., Stancile, G., Schlerf, M., 2022. Multi-sensor spectral synergies for crop stress detection and monitoring in the optical domain: A review. Remote Sens. Environ. 280, 113198.

Calderón, R., Navas-Cortés, J.A., Zarco-Tejada, P.J., 2015. Early detection and quantification of verticillium wilt in olive using hyperspectral and thermal imagery over large areas. Remote Sens. 7 (5), 5584–5610.

Calderón, R., Navas-Cortés, J.A., Lucena, C., Zarco-Tejada, P.J., 2013. High-resolution airborne hyperspectral and thermal imagery for early detection of verticillium wilt of olive using fluorescence, temperature and narrow-band spectral indices. Remote Sens. Environ. 139, 231–245.

Castrignanò, A., Belmonte, A., Antelmi, I., Quarto, R., Quarto, F., Shaddad, S., et al., 2021. Semi-automatic method for early detection of xylella fastidiosa in olive trees using UAV multispectral imagery and geostatistical-discriminant analysis. Rem. Sens. 13, 14.

Cimo, G., Bianco, R.L., Gonzalez, P., Bandaranayake, W., Etxeberria, E., Syvertsen, J.P., 2013. Carbohydrate and nutritional responses to stem girdling and drought stress with respect to understanding symptoms of huanglongbing in citrus. HortScience 48 (7), 920–928.

Daughtry, C.S., Walthall, C.L., Kim, M.S., De Colstoun, E.B., McMurtrey Iii, J.E., 2000. Estimating corn leaf chlorophyll concentration from leaf and canopy reflectance. Remote Sens. Environ. 74 (2), 229–239.

Deering, D.W., 1975. Measuring" forage production" of grazing units from Landsat MSS data. In: Proceedings of the Tenth International Symposium of Remote Sensing of the Environment, pp. 1169–1198.

Di Nisio, A., Adamo, F., Acciani, G., Attivissimo, F., 2020. Fast detection of olive trees affected by xylella fastidiosa from uavs using multispectral imaging. Sensors 20 (17), 4915.

El-Ghany, A., Nesreen, M., El-Aziz, A., Shadia, E., Marei, S.S., 2020. A review: application of remote sensing as a promising strategy for insect pests and diseases management. Environ. Sci. Pollut. Res. 27 (27), 33503–33515.

Féret, J.B., Gitelson, A.A., Noble, S.D., Jacquemoud, S., 2017. PROSPECT-D: towards modeling leaf optical properties through a complete lifecycle. Remote Sens. Environ. 193, 204–215.

Fernández-Escobar, R., De la Rosa, R., Leon, L., Gómez, J.A., Testi, L., Orgaz, F., Gil-Ribes, J.A., Quesada-Moraga, E., Trapero, A., Msallem, M., 2013. Evolution and sustainability of the olive production systems. Opt. Mediterraneennes 106, 11–42.

Fernández-Guisuraga, J.M., Calvo, L., Suárez-Seoane, S., 2020. Comparison of pixel unmixing models in the evaluation of post-fire forest resilience based on temporal series of satellite imagery at moderate and very high spatial resolution. ISPRS J. Photogramm. Remote Sens. 164, 217–228.

Fernández-Guisuraga, J.M., Verrelst, J., Calvo, L., Suárez-Seoane, S., 2021. Hybrid inversion of radiative transfer models based on high spatial resolution satellite reflectance data improves fractional vegetation cover retrieval in heterogeneous ecological systems after fire. Remote Sens. Environ. 255, 112304.

Freeman, E.A., Moisen, G.G., 2008. A comparison of the performance of threshold criteria for binary classification in terms of predicted prevalence and kappa. Ecol. Model. 217 (1–2), 48–58.

Gibin, D., Pasinato, L., Boscia, D., Morelli, M., European Food Safety Authority (EFSA), 2022. Update of the Xylella spp. host plant database–systematic literature search up to 31 December 2021. EFSA Journal 20 (6), e07356.

Gitelson, A.A., 2004. Wide dynamic range vegetation index for remote quantification of biophysical characteristics of vegetation. J. Plant Physiol. 161 (2), 165–173.

Gitelson, A.A., Merzlyak, M.N., 1997. Remote estimation of chlorophyll content in higher plant leaves. Int. J. Remote Sens. 18 (12), 2691–2697.

Gitelson, A.A., Gritz, Y., Merzlyak, M.N., 2003. Relationships between leaf chlorophyll content and spectral reflectance and algorithms for non-destructive chlorophyll assessment in higher plant leaves. J. Plant Physiol. 160 (3), 271–282.

Gitelson, A.A., Viña, A., Ciganda, V., Rundquist, D.C., Arkebauer, T.J., 2005. Remote estimation of canopy chlorophyll content in crops. Geophys. Res. Lett. 32 (8).

Gramaje, D., Pérez-Serrano, V., Montes-Borrego, M., Navas-Cortés, J.A., Jiménez-Díaz, R. M., Landa, B.B., 2013. A comparison of real-time PCR protocols for the quantitative monitoring of asymptomatic olive infections by verticillium dahliae pathotypes. Phytopathology 103 (10), 1058–1068.

Gueymard, C.A., 2001. Parameterized transmittance model for direct beam and circumsolar spectral irradiance. Sol. Energy 71 (5), 325–346.

Haboudane, D., Miller, J.R., Tremblay, N., Zarco-Tejada, P.J., Dextraze, L., 2002. Integrated narrow-band vegetation indices for prediction of crop chlorophyll content for application to precision agriculture. Remote Sens. Environ. 81 (2–3), 416–426.

Hornero, A., Hernández-Clemente, R., North, P.R., Beck, P.S.A., Boscia, D., Navas-Cortes, J.A., Zarco-Tejada, P.J., 2020. Monitoring the incidence of xylella fastidiosa infection in olive orchards using ground-based evaluations, airborne imaging spectroscopy and Sentinel-2 time series through 3-D radiative transfer modelling. Remote Sens. Environ. 236, 111480.

Huang, T., Ding, X., Zhu, X., Chen, S., Chen, M., Jia, X., Lai, F., Zhang, X., 2021. Assessment of poplar looper (Apocheima cinerarius Erschoff) infestation on Euphrates (Populus euphratica) using time-series MODIS NDVI data based on the wavelet transform and discriminant analysis. Remote Sens. 13, 2345.

Huete, A., Didan, K., Miura, T., Rodriguez, E.P., Gao, X., Ferreira, L.G., 2002. Overview of the radiometric and biophysical performance of the MODIS vegetation indices. Remote Sens. Environ. 83 (1–2), 195–213.

Idso, S.B., Jackson, R.D., Pinter Jr., P.J., Reginato, R.J., Hatfield, J.L., 1981. Normalizing the stress-degree-day parameter for environmental variability. Agric. Meteorol. 24, 45–55.

James, G., Witten, D., Hastie, T., 2013. Classification. In: An Introduction to Statistical Learning with Applications in R.

Jiang, Z., Huete, A.R., Didan, K., Miura, T., 2008. Development of a two-band enhanced vegetation index without a blue band. Remote Sens. Environ. 112 (10), 3833–3845.

Jimenez-Diaz, R.M., Cirulli, M., Bubici, G., del Mar Jimenez-Gasco, M., Antoniou, P.P., Tjamos, E.C., 2012. Verticillium wilt, a major threat to olive production: current status and future prospects for its management. Plant Dis. 96 (3), 304–329.

Karpouzli, E., Malthus, T., 2003. The empirical line method for the atmospheric correction of IKONOS imagery. Int. J. Remote Sens. 24 (5), 1143–1150.

Kuter, S., 2021. Completing the machine learning saga in fractional snow cover estimation from MODIS Terra reflectance data: random forests versus support vector regression. Remote Sens. Environ. 255, 112294.

Li, X., Lee, W.S., Li, M., Ehsani, R., Mishra, A.R., Yang, C., Mangan, R.L., 2015. Feasibility study on huanglongbing (citrus greening) detection based on WorldView-2 satellite imagery. Biosyst. Eng. 132, 28–38.
Li, X., Tong, T., Luo, T., Wang, J., Rao, Y., Li, L., Jin, D., Wu, D., Huang, H., 2022. Retrieving the infected area of pine wilt disease-disturbed pine forests from medium-resolution satellite images using the stochastic radiative transfer theory. Remote Sens. 14, 1526.
López-Escudero, F.J., Mercado-Blanco, J., 2011. Verticillium wilt of olive: a case study to implement an integrated strategy to control a soil-borne pathogen. Plant Soil 344 (1), 1–50.
López-Moral, A., Raya-Ortega, M.C., Agustí-Brisach, C., Roca, L.F., Lovera, M., Luque, F., Arquero, O., Trapero, A., 2017. Morphological, pathogenic and molecular characterization of colletotrichum acutatum isolates causing almond anthracnose in Spain. Plant Dis. 101, 2034–2045.
Luisi, N., Ciccarese, F., Sicoli, G., Amenduni, M., 1993. Outbreaks of verticillium wilt on almond and pathogenic variations among isolates of V. Dahliae. In: International Congress on Almond, 373, pp. 287–292.
Main-Knorn, M., Pflug, B., Louis, J., Debaecker, V., Müller-Wilm, U., Gascon, F., 2017, October. Sen2Cor for sentinel-2. In: Image and Signal Processing for Remote Sensing XXIII, Vol. 10427. International Society for Optics and Photonics, p. 1042704.
Mantas, V., Fonseca, L., Baltazar, E., Canhoto, J., Abrantes, I., 2022. Detection of tree decline (Pinus pinaster Aiton) in european forests using Sentinel-2 data. Remote Sens. 14 (9), 2028.
Mantero, P., Moser, G., Serpico, S.B., 2005. Partially supervised classification of remote sensing images through SVM-based probability density estimation. IEEE Trans. Geosci. Remote Sens. 43 (3), 559–570.
Mewes, T., Franke, J., Menz, G., 2011. Spectral requirements on airborne hyperspectral remote sensing data for wheat disease detection. Precis. Agric. 12 (6), 795–812.
Moral, J., Morgan, D., Trapero, A., Michailides, T.J., 2019. Ecology and epidemiology of diseases of nut crops and olives caused by Botryosphaeriaceae fungi in California and Spain. Plant Dis. 103 (8), 1809–1827.
Niblack, W., 1986. In: An introduction to image processing, pp. 115–116.
Özcan, M.M., 2022. A review on some properties of almond: ımpact of processing, fatty acids, polyphenols, nutrients, bioactive properties, and health aspects. J. Food Sci. Technol. 1–12.
Peñuelas, J., Baret, F., Filella, I., 1995. Semi-empirical indices to assess carotenoids/chlorophyll a ratio from leaf spectral reflectance. Photosynthetica 31 (2), 221–230.
Peñuelas, J., Filella, I., Lloret, P., Mun Oz, F., Vilajeliu, M., 1995. Reflectance assessment of mite effects on apple trees. Int. J. Remote Sens. 16 (14), 2727–2733.
Plascyk, J.A., 1975. The MK II Fraunhofer line discriminator (FLD-II) for airborne and orbital remote sensing of solar-stimulated luminescence. Opt. Eng. 14 (4), 144339.
Poblete, T., Camino, C., Beck, P.S.A., Hornero, A., Kattenborn, T., Saponari, M., Boscia, D., Navas-Cortes, J.A., Zarco-Tejada, P.J., 2020. Detection of xylella fastidiosa infection symptoms with airborne multispectral and thermal imagery: assessing bandset reduction performance from hyperspectral analysis. ISPRS J. Photogramm. 162, 27–40.
Poblete, T., Navas-Cortes, J.A., Camino, C., Calderon, R., Hornero, A., Gonzalez-Dugo, V., Landa, B.B., Zarco-Tejada, P.J., 2021. Discriminating xylella fastidiosa from verticillium dahliae infections in olive trees using thermal- and hyperspectral-based plant traits. ISPRS J. Photogramm. 179, 133–144.
Rallo, L., Barranco, D., Díez, C.M., Rallo, P., Suárez, M.P., Trapero, C., Pliego-Alfaro, F., 2018. Strategies for olive (Olea europaea L.) breeding: Cultivated genetic resources and crossbreeding. In: Advances in Plant Breeding Strategies: Fruits. Springer, Cham, pp. 535–600.
Rey, B., Aleixos, N., Cubero, S., Blasco, J., 2019. XF-ROVIM. A field robot to detect olive trees infected by xylella fastidiosa using proximal sensing. Remote Sens. 11 (3), 221.
Ribeiro, R.V., Machado, E.C., Oliveira, R.F., 2003. Early photosynthetic responses of sweet orange plants infected with xylella fastidiosa. Physiol. Mol. Plant Pathol. 62 (3), 167–173.
Richards, J.A., 1999. In: Remote Sensing Digital Image Analysis, vol. 3. Springer, Berlin, pp. 10–38.
Rondeaux, G., Steven, M., Baret, F., 1996. Optimization of soil-adjusted vegetation indices. Remote Sens. Environ. 55 (2), 95–107.
Rouse, J.W., Haas, R.H., Schell, J.A., Deering, W., D., 1974. Monitoring vegetation systems in the great plains with ERTS. NASA Spec. Publ. 351, 309.
Sagan, V., Maimaitijiang, M., Bhadra, S., Maimaitiyiming, M., Brown, D.R., Sidike, P., Fritschi, F.B., 2021. Field-scale crop yield prediction using multi-temporal WorldView-3 and PlanetScope satellite data and deep learning. ISPRS J. Photogramm. Remote Sens. 174, 265–281.
Santoso, H., Tani, H., Wang, X., Prasetyo, A.E., Sonobe, R., 2019. Classifying the severity of basal stem rot disease in oil palm plantations using WorldView-3 imagery and machine learning algorithms. Int. J. Remote Sens. 40 (19), 7624–7646.
Sauvola, J., Pietikäinen, M., 2000. Adaptive document image binarization. Pattern Recogn. 33 (2), 225–236.
Thomas, V.A., Wynne, R.H., Kauffman, J., McCurdy, W., Brooks, E.B., Thomas, R.Q., Rakestraw, J., 2021. Mapping thins to identify active forest management in southern pine plantations using landsat time series stacks. Remote Sens. Environ. 252, 112127.
Tomlinson, C.J., Chapman, L., Thornes, J.E., Baker, C., 2011. Remote sensing land surface temperature for meteorology and climatology: a review. Meteorol. Appl. 18 (3), 296–306.
Torres, M., Pierantozzi, P., Searles, P., Rousseaux, M.C., García-Inza, G., Miserere, A., Bodoira, R., Contreras, C., Maestri, D., 2017. Olive cultivation in the southern hemisphere: flowering, water requirements and oil quality responses to new crop environments. Frontiers. Plant Sci. 8.
Trevethan, R., 2017. Sensitivity, specificity, and predictive values: foundations, pliabilities, and pitfalls in research and practice. Front. Public Health 5, 307.
Tucker, C.J., 1979. Red and photographic infrared linear combinations for monitoring vegetation. Remote Sens. Environ. 8 (2), 127–150.
Vapnik, V., 1999. The nature of statistical learning theory. Springer science & business media.
Verhoef, W., Jia, L., Xiao, Q., Su, Z., 2007. Unified optical-thermal four-stream radiative transfer theory for homogeneous vegetation canopies. IEEE Trans. Geosci. Remote Sens. 45 (6), 1808–1822.
Yang, C., 2020. Remote sensing and precision agriculture technologies for crop disease detection and management with a practical application example. Engineering 6 (5), 528–532.
Zarco-Tejada, P.J., Poblete, T., Camino, C., Gonzalez-Dugo, V., Calderon, R., Hornero, A., Hernandez-Clemente, R., Román-Écija, M., Velasco-Amo, M.P., Landa, B.B., Beck, P. S.A., Saponari, M., Boscia, D., Navas-Cortes, J.A., 2021. Divergent abiotic spectral pathways unravel pathogen stress signals across species. Nat. Commun. 12, 6088.
Zarco-Tejada, P.J., Camino, C., Beck, P.S.A., Calderón, R., Hornero, A., Hernández-Clemente, R., Gonzalez-Dugo, V., North, P.R.J., Landa, B.B., Boscia, D., Saponari, M., Navas-Cortes, J.A., 2018. Previsual symptoms of xylella fastidiosa infection revealed in spectral plant-trait alterations. Nat. Plants 4 (7), 432–439.